

# Wideband Joint Elevation–Azimuth Angle Estimation Based on Multiple Frequency Model and Atomic Norm Minimization

Jingming Zhang<sup>ID</sup>, Min Wu<sup>ID</sup>, *Senior Member, IEEE*, Chengpeng Hao<sup>ID</sup>, *Senior Member, IEEE*,  
and Yongqing Wu<sup>ID</sup>, *Senior Member, IEEE*

**Abstract**—Estimating the direction of arrival (DOA) has been a crucial problem in a wide range of applications. Current research predominantly focuses on narrow-band, 1-D signals, which are not directly applicable to practical scenarios involving wideband and multidimensional signals. To deal with this drawback, we propose a 2-D multiple frequency atomic norm minimization (2DMFANM) algorithm to estimate the elevation and azimuth angles of wideband signals in a grid-less manner. To be specific, we exploit the multiple frequency model to describe the wideband signals and derive the corresponding signal model. Based on the structure of the signal model, we formulated an atomic norm minimization (ANM) problem that allows for the gridless joint estimation of elevation and azimuth angles. The ANM problem is further converted into semidefinite programming (SDP) via analysis of the dual problem. To reduce the computational burden that hinders the deployment of 2DMFANM, we propose two fast algorithms called 2DMFDANM and 2DMFANM\_SizeRedu. Specifically, 2DMFDANM reduces the size of the original algorithm by decoupling the information of spatial angular frequencies, while 2DMFANM\_SizeRedu achieves fast speed by removing the redundancy in the original algorithm. Theoretical and numerical analyses indicate that these two algorithms significantly enhance the speed of computation with minor degradation in the estimation accuracy. Numerical simulations and experimental data analysis demonstrate the superior performance of the proposed methods compared to state-of-the-art algorithms.

**Index Terms**—2-D direction-of-arrival (DOA) estimation, atomic norm minimization (ANM), multiple frequency model, wideband DOA estimation.

## I. INTRODUCTION

**D**IRECTION-of-arrival (DOA) estimation has been a subject of intense research in the field of array signal processing [1], with applications spanning sonar [2], radar [3], and wireless communications [4]. Existing literature primarily focuses on narrow-band and 1-D signals. Although they are

capable of depicting the majority of practical scenes, there still exists a wide range of scenarios where the signals to be processed are wideband and multidimensional [5], [6]. Thus, a considerable number of techniques have been developed to extend the narrow-band, 1-D approaches that are currently in use to wideband and multidimensional contexts.

Wideband signals are usually divided into several subbands and modeled by the multiple frequency model. Signals in each subband can be treated as narrow-band signals, thus, narrow-band algorithms can be utilized. Wax et al. [7] applied subspace methods to each subband independently and proposed the incoherent signal-subspace method (ISSM). However, ISSM overlooked the joint information between subbands, hence the performance degraded. With regard to this limitation, Wang and Kaveh [8] proposed the coherent signal-subspace method (CSSM). The CSSM takes advantage of a focusing matrix to transform different subbands into a reference frequency at which narrow-band techniques can be applied. A class of focusing matrices called rotational signal-subspace (RSS) focusing matrices was then proposed [9].

Some 1-D DOA estimation techniques can be directly employed in 2-D cases with appropriate modifications. To exceed the Rayleigh limit [10], [11], subspace-based methods are widely used in 1-D DOA estimation. The most representative of these are multiple signal classification (MUSIC) [12], [13] and estimation of signal parameters via rotational invariance techniques (ESPRIT) [14]. Hua [15] discovered an enhanced matrix and matrix pencil (MEMP) technique to estimate 2-D spatial frequencies. Incorporating the idea of the matrix pencil with MUSIC, a 2-D MUSIC [16] algorithm was proposed later. Haardt et al. [17] designed the 2-D unitary ESPRIT, which extended ESPRIT to the 2-D case.

The aforementioned algorithms are all covariance-based, which require a sufficient number of samples to yield accurate estimates of the covariance. The performance of such algorithms can be significantly impaired when the sample size is limited. The development of the compressed sensing (CS) theory [18], [19] has led to the application of sparse methods to DOA estimation in recent years [20]. Compared to subspace methods, CS-based methods can recover the desired DOAs with a limited sample size, even in the case of a single snapshot. In their work, Tang et al. [21] employed the  $l_1$ -norm to promote the sparsity of overcomplete dictionaries corresponding to different frequencies. Liu et al. [22] leveraged the sparse Bayesian learning framework, achieving

Received 22 January 2025; accepted 9 March 2025. Date of publication 1 April 2025; date of current version 17 April 2025. This work was supported in part by the National Natural Science Foundation of China under Grant 62371446, Grant 62471463, Grant 62001468, Grant 61971412, and Grant 62201623; and in part by the Youth Innovation Promotion Association CAS under Grant 2023030. The Associate Editor coordinating the review process was Dr. Guglielmo Frigo. (*Corresponding author: Chengpeng Hao.*)

The authors are with the Institute of Acoustics, Chinese Academy of Sciences, Beijing 100190, China, and also with the School of Electronic, Electrical, and Communication Engineering, University of Chinese Academy of Sciences, Beijing 100049, China (e-mail: zhangjingming@mail.ioa.ac.cn; wumin880902@hotmail.com; haochengp@mail.ioa.ac.cn; wyq@mail.ioa.ac.cn).

Digital Object Identifier 10.1109/TIM.2025.3556225

higher estimation accuracy. These aforementioned methods are based on the assumption that the DOAs lie on predefined grids. The instances in which this assumption is not met are known as grid mismatches. Chi et al. [23] conducted an analysis to investigate the influence of grid mismatch and suggested that the performance of the algorithms can be significantly impaired under such circumstances. Zhang et al. [24] demonstrated that grid mismatch could result in target omissions in joint localization and significantly degrade the performance. Various off-grid methods have been proposed to address the problem of grid mismatch [25], [26]. However, these methods still assume the existence of grids, thus, the problem of grid mismatch cannot be completely eliminated.

To address this drawback, several gridless methods have been developed recently. Atomic norm minimization (ANM) [27] methods have become increasingly popular in recent years because they work on continuous dictionaries and can promote sparse representations. Candès and Fernandez-Granda [28] utilized this method to achieve the perfect frequency extension from low-frequency time sampling. Tang et al. [29] explored spectral estimation under random partial observations. Chi and Chen [30] employed the two-level Toeplitz matrix for 2-D extension, while Yang et al. [31] leveraged the multi-level Toeplitz matrix structure for higher-dimensional ANM. To apply the ANM approach to wideband scenarios, Wu et al. [32] took advantage of the multiple frequency model and derived the ANM problem for wideband DOA estimation. The corresponding semidefinite programming (SDP) form was also introduced to facilitate implementation. The algorithm was further extended to the sparse array and MMV cases in [33]. However, the algorithms designed in [32] and [33] are confined to 1-D scenarios and are incompatible with 2-D cases.

This study attempts to apply the ANM approach to wideband 2-D DOA estimation problems. In particular, we consider the problem of estimating the elevation–azimuth angle jointly from the signals received from a planar array. The multiple frequency model was employed to depict wideband signals, and the corresponding signal model was derived. Based on the signal model, we propose a novel atomic set to induce the ANM problem. In order to convert the original ANM problem into a tractable SDP problem, the dual problem was first analyzed. A novel mapping operator was proposed to facilitate the formulation of multivariate trigonometric polynomial inequalities. The bounded lemma [34] was then employed to derive the dual SDP. The primal SDP is derived from the Lagrangian analysis of the dual SDP. Based on the primal SDP, we designed the estimation algorithm 2-D multiple frequency ANM (2DMFANM). Given the significant computational burden associated with 2DMFANM, two additional algorithms were proposed: the decoupled algorithm and the size-reduced algorithm. These were designated as 2DMFDANM and 2DMFANM\_SizeRedu, respectively. Theoretical and simulation analyses of these two algorithms revealed that while the estimation accuracy was slightly degraded compared to the original algorithm, their running speed was significantly improved.

The remainder of this article is organized as follows. Section II introduces the 2-D multifrequency model describing

the signals received. Section III presents the proposed 2DMFANM algorithm and the corresponding fast algorithms 2DMFDANM and 2DMFANM\_SizeRedu. Section IV conducts numerical experiments to demonstrate the superior performance of the proposed algorithms. Section V further validates the effectiveness of the proposed algorithms using the experimental data. Section VI concludes with a discussion of the results and potential avenues for future research.

*Notations:* Matrices and vectors are denoted in bold upper-case letters and bold lowercase letters, respectively.  $(\cdot)^T$  and  $(\cdot)^H$  represent the symmetric transpose and Hermitian transpose.  $\langle \cdot, \cdot \rangle_{\mathbb{R}}$  stands for real inner product. The atomic set is denoted as  $\mathbb{A}$ .  $\otimes$  and  $\odot$  denote Kronecker product and Khatri-Rao product.  $\mathbf{1}$  represents the vector of all ones.  $\mathbf{e}_j$  stands for the vector with the  $j$ th element equal to one.

## II. SIGNAL MODEL

The signal is received through an  $N_1 \times N_2$  uniform rectangular array (URA) with  $K$  far-field wideband waves impinging on it. The array consists of  $N_1$  elements along the  $x$ -axis and  $N_2$  elements along the  $y$ -axis. The elevation and azimuth angles of the  $k$ th wave are denoted by  $\theta_k$  and  $\phi_k$ , respectively, as illustrated in Fig. 1. The wideband source signal can be represented by the multiple frequency model using off-the-shelf spectral analysis techniques, such as the discrete Fourier transform (DFT) and filter bank methods [32], [33], [35], [36]. Assume a total of  $N_f$  subbands, with the central frequency of each subband defined as  $f \cdot f_0$ , where  $f \in \{1, 2, \dots, N_f\}$ . The  $i$ th source signal  $s_i$  can then be expressed as

$$s_i = c_i \cdot [p_{\omega_i}^1, p_{\omega_i}^2, \dots, p_{\omega_i}^{N_f}] = c_i \mathbf{p}_{\omega_i}^T \quad (1)$$

where  $\mathbf{p}_{\omega_i}^T \triangleq [p_{\omega_i}^1, p_{\omega_i}^2, \dots, p_{\omega_i}^{N_f}]$ ,  $\|\mathbf{p}_{\omega_i}\| = 1$ . Here,  $c_i$  represents the signal amplitude, and  $\mathbf{p}_{\omega_i}$  comprises the power across  $N_f$  frequency bins. Let  $J$  be the set of array element indices, defined as  $J = \{0, 1, \dots, N_1 - 1\} \times \{0, 1, \dots, N_2 - 1\}$ . The signal received by the  $k$ th element in the  $f$ th subband can then be expressed as

$$y_k^f = x_k^f + n_k^f \quad (2)$$

$$\begin{aligned} x_k^f &= x_{(k_1, k_2)}^f \\ &= \sum_{i=1}^r c_i \exp\left(j2\pi f \frac{d}{c} [\cos(\phi_i) \sin(\theta_i), \sin(\phi_i) \sin(\theta_i)] \mathbf{k}\right) \\ &\quad \cdot p_{\omega_i}^f \end{aligned} \quad (3)$$

where  $\mathbf{k} = [k_1, k_2]^T \in J$ ,  $c$  denotes the wave velocity,  $d$  is the interspacing of the array elements, and  $n_k^f$  is the noise received by the element.

Define the angular frequency vector as  $\omega_i = [\omega_{1i}, \omega_{2i}]^T \triangleq f_0(d/c)[\cos(\phi_i) \sin(\theta_i), \sin(\phi_i) \sin(\theta_i)]^T$ , we have

$$x_k^f = x_{(k_1, k_2)}^f = \sum_{i=1}^r c_i \exp(j2\pi f \omega_i^T \mathbf{k}) \cdot p_{\omega_i}^f. \quad (4)$$

Angular information comprising the elevation and azimuth angles can be retrieved by accurately determining  $\omega_i$ . To be specific, we have

$$\theta = \arcsin\left(\sqrt{\omega_1^2 + \omega_2^2} \cdot \frac{c}{f_0 d}\right) \quad (5)$$

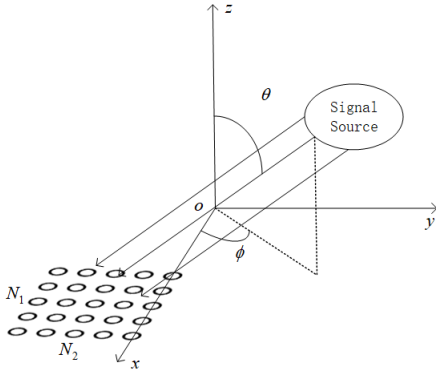


Fig. 1. Geometry of array configuration.

and

$$\phi = \arctan\left(\frac{\omega_2}{\omega_1}\right). \quad (6)$$

Combining signals calculated from  $N_f$  subbands, the signal received by the  $k$ th element can be put together as

$$\mathbf{y}_k = [y_k^1, y_k^2, \dots, y_k^f] = \mathbf{x}_k + \mathbf{n}_k \quad (7)$$

where

$$\begin{aligned} \mathbf{x}_k &= [x_k^1, x_k^2, \dots, x_k^f] \\ &= \sum_{i=1}^r c_i \cdot [\exp(j2\pi\omega_i^T \mathbf{k}), \dots, \exp(j2\pi N_f \omega_i^T \mathbf{k})] \odot \mathbf{p}_{\omega_i}^T. \end{aligned} \quad (8)$$

When the signals received by all array elements on the  $f$ th subband are aggregated, the resulting matrix representation is as follows:

$$\mathbf{Y}^f = [\mathbf{y}_k^f] = \mathbf{X}^f + \mathbf{N}^f \quad (9)$$

where  $\mathbf{X}^f = [\mathbf{x}_k^f]$ .

$\mathbf{X}^f$  can be further expressed as

$$\begin{aligned} \mathbf{X}^f &= \sum_{i=1}^r (c_i \mathbf{p}_{\omega_i}^f) \cdot \mathbf{a}_2(f, \omega_{2i}) \mathbf{a}_1(f, \omega_{1i})^T \\ &= \sum_{i=1}^r (c_i \mathbf{p}_{\omega_i}^f) \mathbf{A}(f, \omega_i) \end{aligned} \quad (10)$$

where  $\mathbf{a}_k(f, \omega_{ki}) = [1, \exp(j2\pi f \omega_{ki}), \dots, \exp(j2\pi f \omega_{ki} \cdot (N_k - 1))]$ , for  $k = 1, 2$ , represent the steering vectors. The matrix  $\mathbf{A}(f, \omega_i)$  is defined as:  $\mathbf{A}(f, \omega_i) = \mathbf{a}_2(f, \omega_{2i}) \cdot \mathbf{a}_1(f, \omega_{1i})^T$ . Vectorizing equation (10) leads to the following representation of the  $f$ th subband:

$$\tilde{\mathbf{x}}^f \triangleq \text{vec}(\mathbf{X}^f) = \sum_{i=1}^r (c_i \mathbf{p}_{\omega_i}^f) \mathbf{a}_1(f, \omega_{1i}) \otimes \mathbf{a}_2(f, \omega_{2i}). \quad (11)$$

By integrating equations (8) and (11), we obtain the complete signal model

$$\begin{aligned} \tilde{\mathbf{X}} &\triangleq [\tilde{\mathbf{x}}^1, \tilde{\mathbf{x}}^2, \dots, \tilde{\mathbf{x}}^{N_f}] \\ &= \sum_{i=1}^r c_i [\tilde{\mathbf{a}}(1, \omega_i), \tilde{\mathbf{a}}(2, \omega_i), \dots, \tilde{\mathbf{a}}(N_f, \omega_i)] \odot \mathbf{p}_{\omega_i}^T \\ &= \sum_{i=1}^r c_i \tilde{\mathbf{A}}(\omega_i) \odot \mathbf{p}_{\omega_i}^T \end{aligned} \quad (12)$$

where  $\tilde{\mathbf{A}}(\omega_i) \triangleq [\tilde{\mathbf{a}}(1, \omega_i), \tilde{\mathbf{a}}(2, \omega_i), \dots, \tilde{\mathbf{a}}(N_f, \omega_i)]$ . Correspondingly, when noise is present, we have

$$\tilde{\mathbf{Y}} = [\text{vec}(\mathbf{Y}^1), \dots, \text{vec}(\mathbf{Y}^{N_f})] = \tilde{\mathbf{X}} + \tilde{\mathbf{N}} \quad (13)$$

where  $\tilde{\mathbf{N}} = [\text{vec}(\mathbf{N}^1), \dots, \text{vec}(\mathbf{N}^{N_f})]$ .

In this article,  $\tilde{\mathbf{Y}}$  represents the signal from which the desired DOA information was to be extracted.

### III. ALGORITHMS

#### A. 2DMFANM Algorithm

In this section, we present our original 2DMFANM algorithm and its application to the joint elevation-azimuth angle estimation.

Inspired by the form of (12), we define the atomic set  $\mathbb{A}$  as follows:

$$\mathbb{A} \triangleq \{\tilde{\mathbf{A}}(\omega) \odot \mathbf{p}_{\omega}^T | \omega \in [0, 1]^2, \|\mathbf{p}_{\omega}\|_2 = 1\}. \quad (14)$$

$\mathbb{A}$  encompasses all the possible steering vectors modulated by the power pattern vector  $\mathbf{p}_{\omega}$ . Without loss of generality,  $\mathbf{p}_{\omega}$  is normalized to obtain a unit Euclidean norm.

To extract DOA information from the observed signal  $\tilde{\mathbf{Y}}$ , the proposed ANM problems are formulated as follows.

For the noise-free case

$$\min_{\tilde{\mathbf{X}}} \|\tilde{\mathbf{X}}\|_{\mathbb{A}}, \quad \text{s.t. } \tilde{\mathbf{Y}} = \tilde{\mathbf{X}}. \quad (15)$$

For the noise-present case

$$\min_{\tilde{\mathbf{X}}} \|\tilde{\mathbf{X}}\|_{\mathbb{A}}, \quad \text{s.t. } \|\tilde{\mathbf{Y}} - \tilde{\mathbf{X}}\|_2 \leq \beta \quad (16)$$

where  $\beta$  represents noise power. Here, the atomic norm  $\|\tilde{\mathbf{X}}\|_{\mathbb{A}}$  is defined as

$$\begin{aligned} \|\tilde{\mathbf{X}}\|_{\mathbb{A}} &= \inf\{t \geq 0 | \tilde{\mathbf{X}} \in t \cdot \text{conv}(\mathbb{A})\} \\ &= \inf\left\{\sum_{\omega} |c_{\omega}| \|\tilde{\mathbf{X}}\|_{\mathbb{A}} = \sum_{\omega} c_{\omega} \tilde{\mathbf{A}}(\omega) \odot \mathbf{p}_{\omega}^T\right\}. \end{aligned} \quad (17)$$

The objective in the noise-free case is to find the sparsest representation of  $\tilde{\mathbf{Y}}$  using atoms in  $\mathbb{A}$ . In the noise-present case, the objective is to find a representation that is both sparse and within a certain error tolerance  $\beta$  for the noisy observation  $\tilde{\mathbf{Y}}$ .

Given that the atomic norm cannot be computed directly, the optimization problem must be reformulated as an SDP problem to enable a solution. The subsequent portion of this section details the conversion process of (15), pertaining to the noise-free case, into an SDP. Similarly, (16) that addresses the case with noise can be transformed into an SDP using a similar process.

The dual problem of (15) is

$$\max_{\mathbf{Q}} \langle \tilde{\mathbf{Y}}, \mathbf{Q} \rangle_{\mathbb{R}}, \quad \text{s.t. } \|\mathbf{Q}\|_{\mathbb{A}}^* \leq 1 \quad (18)$$

where  $\|\cdot\|_{\mathbb{A}}^*$  is the dual norm of the atomic norm defined in (17), which is defined as

$$\|\mathbf{Q}\|_{\mathbb{A}}^* = \sup_{\|\tilde{\mathbf{X}}\|_{\mathbb{A}} \leq 1} \langle \mathbf{Q}, \tilde{\mathbf{Y}} \rangle_{\mathbb{R}}. \quad (19)$$

Utilizing the definition of  $\tilde{\mathbf{X}}$  in (12) and defining  $\mathbf{Q} = [\mathbf{q}_1, \mathbf{q}_2, \dots, \mathbf{q}_{N_f}]$ , it yields

$$\begin{aligned} \|\mathbf{Q}\|_{\mathbb{A}}^* &= \sup_{\|\tilde{\mathbf{X}}\|_{\mathbb{A}} \leq 1} \langle \mathbf{Q}, \tilde{\mathbf{Y}} \rangle_{\mathbb{R}} \\ &= \sup_{\omega, p_{\omega}} \langle \mathbf{Q}, \tilde{\mathbf{A}}(\omega) \odot \mathbf{p}_{\omega}^T \rangle_{\mathbb{R}} \\ &= \sup_{\omega, p_{\omega}} \operatorname{Re} \left( \sum_{f=1}^{N_f} p_{\omega}^f \mathbf{q}_f^H \tilde{\mathbf{a}}(f, \omega) \right). \end{aligned} \quad (20)$$

Let  $\Psi(\mathbf{Q}, \omega) \triangleq [\mathbf{q}_1^H \tilde{\mathbf{a}}(1, \omega), \dots, \mathbf{q}_{N_f}^H \tilde{\mathbf{a}}(N_f, \omega)]^T$ . We obtain

$$\begin{aligned} \|\mathbf{Q}\|_{\mathbb{A}}^* &= \sup_{p_{\omega}, \omega} \operatorname{Re}(\mathbf{p}_{\omega}^H \Psi(\mathbf{Q}, \omega)) \\ &= \sup_{p_{\omega}, \omega} |\mathbf{p}_{\omega}^H \Psi(\mathbf{Q}, \omega)| \\ &= \sup_{\omega} \|\Psi(\mathbf{Q}, \omega)\|_2. \end{aligned} \quad (21)$$

In order to write  $\|\Psi(\mathbf{Q}, \omega)\|$  in the form of a multivariate trigonometric polynomial to which the bounded lemma [34] can be applied to derive an SDP, it is necessary to define a suitable mapping operator. Inspired by the mapping operator proposed in [32], we introduce a mapping operator for 2-D signals. Let

$$\begin{aligned} \mathbf{A}_1(\omega_1) &\triangleq [\mathbf{a}_1(1, \omega_1), \mathbf{a}_1(2, \omega_1), \dots, \mathbf{a}_1(N_f, \omega_1)] \\ \mathbf{A}_2(\omega_2) &\triangleq [\mathbf{a}_2(1, \omega_2), \mathbf{a}_2(2, \omega_2), \dots, \mathbf{a}_2(N_f, \omega_2)]. \end{aligned} \quad (22)$$

By definition of  $\tilde{\mathbf{A}}(\omega)$ , we have

$$\tilde{\mathbf{A}}(\omega) = \mathbf{A}_1(\omega_1) \odot \mathbf{A}_2(\omega_2). \quad (23)$$

To construct the desired mapping operator, we make the following definitions:

$$\begin{aligned} \mathbf{z}_1 &= \mathbf{z}_1(\omega_1) \triangleq [1, \exp(j2\pi\omega_1), \dots, \exp(j2\pi\omega_1 N_f(N_1 - 1))]^T \\ \mathbf{z}_2 &= \mathbf{z}_2(\omega_2) \triangleq [1, \exp(j2\pi\omega_2), \dots, \exp(j2\pi\omega_2 N_f(N_2 - 1))]^T \end{aligned} \quad (24)$$

where  $\mathbf{z}_1 \in \mathbb{C}^{\tilde{N}_1}$ ,  $\mathbf{z}_2 \in \mathbb{C}^{\tilde{N}_2}$ ,  $\tilde{N}_1 \triangleq N_f(N_1 - 1) + 1$ ,  $\tilde{N}_2 \triangleq N_f(N_2 - 1) + 1$ . Let

$$\begin{aligned} \mathbf{Z}_1 &= \mathbf{Z}_1(\omega_1) \triangleq [\mathbf{z}_1, \mathbf{z}_1, \dots, \mathbf{z}_1] \in \mathbb{C}^{\tilde{N}_1 \times N_f} \\ \mathbf{Z}_2 &= \mathbf{Z}_2(\omega_2) \triangleq [\mathbf{z}_2, \mathbf{z}_2, \dots, \mathbf{z}_2] \in \mathbb{C}^{\tilde{N}_2 \times N_f} \end{aligned} \quad (25)$$

and

$$\mathbf{Z} = \mathbf{Z}(\omega) \triangleq \mathbf{Z}_1(\omega_1) \odot \mathbf{Z}_2(\omega_2) = [\mathbf{z}, \mathbf{z}, \dots, \mathbf{z}] \in \mathbb{C}^{\tilde{N}_1 \tilde{N}_2 \times N_f} \quad (26)$$

where  $\mathbf{z} \triangleq \mathbf{z}_1 \otimes \mathbf{z}_2$ .

Upon examining equations (23) through (26), it becomes apparent that  $\tilde{\mathbf{A}}(\omega)$  may be regarded as a partial observation of  $\tilde{\mathbf{Z}}(\omega)$ . Consequently, we propose the mapping operator  $\mathcal{R}$  such that

$$\tilde{\mathbf{A}} = \mathcal{R}(\tilde{\mathbf{Z}}), \quad \mathcal{R} : \mathbb{C}^{\tilde{N}_1 \tilde{N}_2 \times N_f} \rightarrow \mathbb{C}^{N_1 N_2 \times N_f} \quad (27)$$

where

$$[\mathcal{R}(\tilde{\mathbf{Z}})]_{(i-1)N_1+j, f} = \tilde{\mathbf{Z}}_{(i-1)\tilde{N}_1+(j-1)f+1, f}. \quad (28)$$

Let

$$\tilde{\mathbf{X}}' \triangleq \sum_{\omega} c_{\omega} \mathbf{Z}(\omega) \odot \mathbf{p}_{\omega}^H. \quad (29)$$

It yields from (12), (27), and (29) that  $\tilde{\mathbf{X}} = \mathcal{R}(\tilde{\mathbf{X}}')$ . Let

$$\begin{aligned} \mathbf{H} &= \mathcal{R}^*(\mathbf{Q}) \\ \mathbf{Q} &= \mathcal{R}(\mathbf{H}). \end{aligned} \quad (30)$$

Substitute (30) into the definition of  $\Psi(\mathbf{Q}, \omega)$ , we obtain

$$\Psi(\mathbf{Q}, \omega) = \mathbf{H}^H \mathbf{z}. \quad (31)$$

(21) thus becomes

$$\|\mathbf{Q}\|_{\mathbb{A}}^* = \sup_{\omega} \|\mathbf{H}^H \mathbf{z}\|_2 \quad (32)$$

which shows that

$$\|\mathbf{Q}\|_{\mathbb{A}}^* \leq 1 \Leftrightarrow \|\mathbf{H}^H \mathbf{z}\|_2 \leq 1 \quad \forall \omega. \quad (33)$$

It is important to note that the right-hand side of (33) constitutes a multivariate trigonometric polynomial inequality. By invoking the bounded lemma [34] for multivariate trigonometric polynomials and applying an appropriate sum-of-squares relaxation, this inequality can be reformulated into the subsequent SDP problem

$$\begin{aligned} \delta_k &= \operatorname{Tr}[\Theta_k \mathbf{P}_0], \quad k \in \mathcal{H} \\ \begin{bmatrix} \mathbf{P}_0 & \mathbf{H} \\ \mathbf{H}^H & \mathbf{I}_{N_f} \end{bmatrix} &\succcurlyeq 0 \end{aligned} \quad (34)$$

where  $\mathcal{H}$  is half-space,  $\Theta_k = \Theta_{k_1} \otimes \Theta_{k_2}$ ,  $\mathbf{k} = [k_1, k_2]$ .  $\Theta_{k_i}$  is an  $\tilde{N}_i \times \tilde{N}_i$  Toeplitz matrix with ones on the  $k_i$ th diagonal and 0 elsewhere,  $i = 1, 2$ . Then, (18) can be converted into an SDP as follows:

$$\begin{aligned} \max_{\mathbf{Q}, \mathbf{P}_0, \mathbf{H}} & \langle \tilde{\mathbf{Y}}, \mathbf{Q} \rangle_{\mathbb{R}} \\ \text{s.t. } & \delta_k = \operatorname{Tr}[\Theta_k \mathbf{P}_0], \quad k \in \mathcal{H} \\ & \begin{bmatrix} \mathbf{P}_0 & \mathbf{H} \\ \mathbf{H}^H & \mathbf{I}_{N_f} \end{bmatrix} \succcurlyeq 0 \\ & \mathbf{H} = \mathcal{R}^*(\mathbf{Q}). \end{aligned} \quad (35)$$

Through the standard Lagrangian dual analysis, the SDP formulation of the primal problem (15) can be derived from the dual problem of (35).

The Lagrangian function of (35) is

$$\begin{aligned} \mathcal{L}(\mathbf{Q}, \mathbf{P}_0, \mathbf{H}, \Lambda_1, \Lambda_2, \Lambda_3, \Lambda_Q, \nu) &= \langle \tilde{\mathbf{Y}}, \mathbf{Q} \rangle_{\mathbb{R}} + \left\langle \begin{bmatrix} \Lambda_1 & \Lambda_2 \\ \Lambda_2^H & \Lambda_3 \end{bmatrix}, \begin{bmatrix} \mathbf{P}_0 & \mathbf{H} \\ \mathbf{H}^H & \mathbf{I}_{N_f} \end{bmatrix} \right\rangle_{\mathbb{R}} \\ &+ \operatorname{Re} \left\{ \sum_{k \in \mathcal{H}} \nu_k (\delta_k - \operatorname{Tr}[\Theta_k \mathbf{P}_0]) \right\} - \langle \Lambda_Q, \mathbf{H} - \mathcal{R}^*(\mathbf{Q}) \rangle_{\mathbb{R}} \\ &= \langle \tilde{\mathbf{Y}}, \mathbf{Q} \rangle_{\mathbb{R}} + \langle \Lambda_Q, \mathcal{R}^*(\mathbf{Q}) \rangle_{\mathbb{R}} + \langle \mathbf{P}_0, \Lambda_1 \rangle_{\mathbb{R}} + 2\langle \Lambda_2, \mathbf{H} \rangle_{\mathbb{R}} \\ &+ \operatorname{Tr}(\Lambda_3) + \nu_0 - \langle \Lambda_Q, \mathbf{H} \rangle_{\mathbb{R}} - \langle \mathbf{P}_0, \mathbf{Toep}_{2D}(\nu) \rangle_{\mathbb{R}} \end{aligned} \quad (36)$$



where  $\Lambda_1, \Lambda_2, \Lambda_3, \Lambda_Q$  and  $\mathbf{v}$  are dual variables.  $\mathbf{Toep}_{2D}$  is a 2-D Toeplitz operator that transforms  $\mathbf{v} = [\mathbf{v}]_k$  into a 2-level Toeplitz matrix. The dual function is

$$\begin{aligned} g(\Lambda_1, \Lambda_2, \Lambda_3, \Lambda_Q, \mathbf{v}) \\ = \sup_{\mathbf{Q}, \mathbf{P}_0, \mathbf{H}} \mathcal{L}(\mathbf{Q}, \mathbf{P}_0, \mathbf{H}, \Lambda_1, \Lambda_2, \Lambda_3, \Lambda_Q, \mathbf{v}) \\ \text{s.t. } \begin{bmatrix} \Lambda_1 & \Lambda_2 \\ \Lambda_2^H & \Lambda_3 \end{bmatrix} \succcurlyeq 0. \end{aligned} \quad (37)$$

Let

$$\begin{aligned} J(\mathbf{Q}) &\triangleq \langle \tilde{\mathbf{Y}}, \mathbf{Q} \rangle_{\mathbb{R}} + \langle \Lambda_Q, \mathcal{R}^*(\mathbf{Q}) \rangle_{\mathbb{R}} \\ &= \langle \mathcal{R}(\Lambda_Q) + \tilde{\mathbf{Y}}, \mathbf{Q} \rangle_{\mathbb{R}} \\ J(\mathbf{P}_0) &\triangleq \langle \mathbf{P}_0, \Lambda_1 \rangle_{\mathbb{R}} - \langle \mathbf{P}_0, \mathbf{Toep}_{2D}(\mathbf{v}) \rangle_{\mathbb{R}} \\ &= \langle \mathbf{P}_0, \Lambda_1 - \mathbf{Toep}_{2D}(\mathbf{v}) \rangle_{\mathbb{R}} \\ J(\mathbf{H}) &\triangleq 2\langle \Lambda_2, \mathbf{H} \rangle_{\mathbb{R}} - \langle \Lambda_Q, \mathbf{H} \rangle_{\mathbb{R}} \\ &= \langle 2\Lambda_2 - \Lambda_Q, \mathbf{H} \rangle_{\mathbb{R}}. \end{aligned} \quad (38)$$

Substitute (38) into (37), we have

$$\begin{aligned} g(\Lambda_1, \Lambda_2, \Lambda_3, \Lambda_Q, \mathbf{v}) &= \sup_{\mathbf{Q}, \mathbf{P}_0, \mathbf{H}} J(\mathbf{Q}) + J(\mathbf{P}_0) + J(\mathbf{H}) \\ &\quad + \text{Tr}(\Lambda_3) + \mathbf{v}_0, \quad \text{s.t. } \begin{bmatrix} \Lambda_1 & \Lambda_2 \\ \Lambda_2^H & \Lambda_3 \end{bmatrix} \\ &\succcurlyeq 0. \end{aligned} \quad (39)$$

The supremum of  $J(\mathbf{Q})$ ,  $J(\mathbf{P}_0)$  and  $J(\mathbf{H})$  exists if and only if  $\tilde{\mathbf{Y}} = -\mathcal{R}(\Lambda_Q)$ ,  $\mathbf{Toep}_{2D}(\mathbf{v}) = \Lambda_1 \succcurlyeq 0$  and  $\Lambda_Q = -2\Lambda_2$ . Let  $\tilde{\mathbf{X}}^\star = -\Lambda_Q$ ,  $\Lambda_3 = (1/2)\mathbf{W}$  and  $\mathbf{v} = (1/2)\boldsymbol{\mu}$ , the primal SDP can be formulated as

$$\begin{aligned} \min_{\mathbf{W}, \boldsymbol{\mu}, \tilde{\mathbf{X}}^\star} & \frac{1}{2} [\text{Tr}(\mathbf{W}) + \text{Tr}(\mathbf{Toep}_{2D}(\boldsymbol{\mu}))] \\ \text{s.t. } & \begin{bmatrix} \mathbf{Toep}_{2D}(\boldsymbol{\mu}) & \tilde{\mathbf{X}}^\star \\ \tilde{\mathbf{X}}^{\star H} & \mathbf{W} \end{bmatrix} \succcurlyeq 0 \\ & \tilde{\mathbf{Y}} = \mathcal{R}(\tilde{\mathbf{X}}^\star) \end{aligned} \quad (40)$$

where  $\mathbf{Toep}_{2D}(\boldsymbol{\mu})$  is a two-level Toeplitz matrix and  $\boldsymbol{\mu} \in \mathbb{C}^{\tilde{N}_1 \times \tilde{N}_2}$ . In the scenario that noise is present, the primal SDP is modified as follows:

$$\begin{aligned} \min_{\mathbf{W}, \boldsymbol{\mu}, \tilde{\mathbf{X}}^\star} & \frac{1}{2} [\text{Tr}(\mathbf{W}) + \text{Tr}(\mathbf{Toep}_{2D}(\boldsymbol{\mu}))] \\ \text{s.t. } & \begin{bmatrix} \mathbf{Toep}_{2D}(\boldsymbol{\mu}) & \tilde{\mathbf{X}}^\star \\ \tilde{\mathbf{X}}^{\star H} & \mathbf{W} \end{bmatrix} \succcurlyeq 0 \\ & \|\tilde{\mathbf{Y}} - \mathcal{R}(\tilde{\mathbf{X}}^\star)\|_2 \leq \epsilon. \end{aligned} \quad (41)$$

The angular frequency vector  $\boldsymbol{\omega} = [\omega_1, \omega_2]$  can be extracted from  $\mathbf{Toep}_{2D}(\boldsymbol{\mu})$  using the MaPP technique, as proposed in [31]. Subsequently, the elevation and azimuth angles can be estimated using (5) and (6), respectively. The complete algorithm is summarized in Algorithm 1.

It is worth noting that the positive semi-definite (P.S.D) matrices in (34) and (35) have a size of  $((N_f(N_1 - 1) + 1)(N_f(N_2 - 1) + 1) + N_f) \times ((N_f(N_1 - 1) + 1)(N_f(N_2 - 1) + 1) + N_f)$  and contain  $O((N_1 N_2 N_f^2)^2)$  elements. This can cause significant computational burdens and hinder the implementation of the algorithm in practical scenarios where computational resources are limited. Consequently, the design

#### Algorithm 1 2DMFANM

---

**Input:**  $\{\mathbf{Y}^f\}_{f=1}^{N_f}, N_1, N_2, N_f, \epsilon$   
**Output:**  $\{[\theta_i, \phi_i]\}_{i=1}^K$

- 1  $\tilde{\mathbf{Y}} \leftarrow [\text{vec}(\mathbf{Y}^1), \dots, \text{vec}(\mathbf{Y}^{N_f})];$
- 2 **for**  $k=1:2$  **do**
- 3    $\tilde{N}_k = N_f(N_k - 1) + 1;$
- 4 Construct mapping operator  $R$  in accordance with (28);
- 5 **if** noise-free **then**
- 6   Solve (40);
- 7 **else**
- 8   Solve (41);
- 9  $\{[\omega_{1i}, \omega_{2i}]\}_{i=1}^K \leftarrow \text{MaPP}(\mathbf{Toep}_{2D}(\boldsymbol{\mu}));$
- 10  $\theta = \arcsin(\sqrt{\omega_1^2 + \omega_2^2 \cdot \frac{c}{f_0 d}}), \phi = \arctan(\frac{\omega_2}{\omega_1});$

---

of fast algorithms is essential. Upon examination of (34) and (35), the considerable size of P.S.D matrices can be attributed to two primary factors. The first factor is that the constructed mapping operator is too “loose,” which results in the all-zero rows in  $\mathbf{H}$  in (34) and fully undetermined rows in  $\tilde{\mathbf{X}}^\star$  in (40). This leads to large size of the P.S.D matrices, as previously noted in [32]. The second factor is that the two spatial angular frequencies are coupled by the Kronecker product in (11), which results in the large-scale two-level Toeplitz matrix in (40). The remainder of this section will be devoted to addressing the computational problems from these two perspectives. To address the first issue, we propose a size-reduced algorithm, designated 2DMFANM\_SizeRedu, which is designed to reduce the size of the matrix. To handle the second issue, we propose a decoupled algorithm, designated as 2DMFDANM, to decouple the matrix.

#### B. Decoupled Algorithm—2DMFDANM

In order to decouple the spatial angular frequencies  $\omega_1$  and  $\omega_2$ , the data collected in (12) and (13) are rearranged in  $\mathbf{Y}_2 \in \mathbb{C}^{N_2 \times N_1 \times N_f}$  and  $\mathbf{Y}_1 \in \mathbb{C}^{N_1 \times N_2 \times N_f}$ , which are defined as follows:

$$\begin{aligned} [\mathbf{Y}_2]_{::,f} &= \mathbf{Y}^f \\ [\mathbf{Y}_1]_{::,f} &= [\mathbf{Y}^f]^T \end{aligned} \quad (42)$$

where  $\mathbf{Y}^f$  is defined in (9).

A straightforward decoupling scheme is to view  $\mathbf{Y}_1$  and  $\mathbf{Y}_2$  as two 1-D multiple measurement vector multifrequency (MMV-MF) measurements, as defined in [33]. Here,  $\mathbf{Y}_1$  measures the spatial angular frequency  $\omega_1$  and  $\mathbf{Y}_2$  measures  $\omega_2$ . As outlined in [33], the angular frequencies,  $\omega_1$  and  $\omega_2$ , can be retrieved via certain optimization programs [see (76)].

Since  $\omega_1$  and  $\omega_2$  are decoupled in the previous step, a pairing step is unavoidable to extract the correct spatial angular frequencies. A pairing algorithm called MFPairing is proposed as follows. Suppose the decoupled estimations  $\{\hat{\omega}_{1i}\}_{i=1}^{K_1}$  and  $\{\hat{\omega}_{2i}\}_{i=1}^{K_2}$  are available, according to (10), we have

$$\begin{aligned} \exists \mathbf{S}^f &\in \mathbb{C}^{K_2 \times K_1}, \quad \text{s.t.} \\ \mathbf{X}^f &= \mathbf{A}_2(f, \hat{\omega}_2) \mathbf{S}^f \mathbf{A}_1(f, \hat{\omega}_1)^T, \quad f = 1, 2, \dots, N_f \end{aligned} \quad (43)$$

where  $\mathbf{A}_k(f, \hat{\omega}_k) = [\mathbf{a}_k(f, \hat{\omega}_{k1}), \dots, \mathbf{a}_k(f, \hat{\omega}_{kr_k})]$ ,  $k = 1, 2$ . We further have

$$\text{vec}(\mathbf{X}^f) = \mathbf{A}_1(f, \hat{\omega}_1) \otimes \mathbf{A}_2(f, \hat{\omega}_2) \text{vec}(\mathbf{S}^f). \quad (44)$$

It is important to note that the non-zero entries among all  $\{\mathbf{S}^f\}_{f=1}^{N_f}$  share the same indices. Consequently, the following optimization program was designed to pair the spatial angular frequencies:

$$\begin{aligned} \tilde{\mathbf{S}}^* &= \arg \min_{\tilde{\mathbf{S}}} \|\tilde{\mathbf{S}}\|_{2,1} \\ \text{s.t. } &\|\text{vec}(\mathbf{X}^f) - \mathbf{A}_1(f, \hat{\omega}_1) \otimes \mathbf{A}_2(f, \hat{\omega}_2) \text{vec}(\mathbf{S}^f)\| \\ &\leq \epsilon, \quad f = 1, \dots, N_f \\ \tilde{\mathbf{S}} &= [\text{vec}(\mathbf{S}^1), \dots, \text{vec}(\mathbf{S}^{N_f})]. \end{aligned} \quad (45)$$

Normalizing every column in  $\tilde{\mathbf{S}}$  yields  $\tilde{\mathbf{S}}'$ . Let  $\tilde{\mathbf{s}} = \tilde{\mathbf{S}}' \cdot \mathbf{1}_{N_f}$ . The final stage of the pairing process involves selecting the largest  $K$  elements in  $\tilde{\mathbf{s}}$ . These indices indicate the desired pairs. The corresponding algorithm is summarized in Algorithm 2. The complete decoupled algorithm is presented in Algorithm 3.

Although the decoupling scheme is relatively straightforward, the numerical simulations presented in Section IV have demonstrated that the accuracy achieved may not be satisfactory. One main reason for this is that the interdependent relationship between  $\omega_1$  and  $\omega_2$  is entirely lost when viewing 2-D signals as 1-D. In light of this joint relationship, we propose the following decoupled algorithm.

Let  $\mathbf{X} = [\mathbf{X}^1, \mathbf{X}^2, \dots, \mathbf{X}^{N_f}]$ . With the help of (24), we define  $\tilde{\mathbf{X}}^f \in \mathbb{C}^{\tilde{N}_2 \times \tilde{N}_1}$  as

$$\begin{aligned} \tilde{\mathbf{X}}^f &= \sum_{i=1}^r (c_i p_{\omega_i}^f) \cdot \mathbf{z}_2(\omega_2) \mathbf{z}_1(\omega_1)^T \\ &= \sum_{i=1}^r (c_i p_{\omega_i}^f) \cdot \mathbf{z}_2(\omega_2) \mathbf{z}_1(-\omega_1)^H. \end{aligned} \quad (46)$$

It is easy to construct a mapping operator  $\mathcal{R}_d^f$  such that

$$\mathbf{X}^f = \mathcal{R}_d^f(\tilde{\mathbf{X}}^f), \quad \mathcal{R}_d^f: \mathbb{C}^{\tilde{N}_2 \times \tilde{N}_1} \rightarrow \mathbb{C}^{N_2 \times N_1} \quad (47)$$

where

$$[\mathcal{R}_d^f(\tilde{\mathbf{X}}^f)]_{i,j} = \tilde{\mathbf{X}}_{(i-1)f+1, (j-1)f+1}^f. \quad (48)$$

Let  $\tilde{\mathbf{X}} = [\tilde{\mathbf{X}}^1, \dots, \tilde{\mathbf{X}}^{N_f}]$ , a corresponding mapping operator  $\mathcal{R}_d: \mathbb{C}^{\tilde{N}_2 \times \tilde{N}_1 N_f} \rightarrow \mathbb{C}^{N_2 \times N_1 N_f}$  can be designed as

$$[\mathcal{R}_d(\tilde{\mathbf{X}})]_{:, N_1(f-1)+1: N_1 f} = \mathcal{R}_d^f(\tilde{\mathbf{X}}_{:, \tilde{N}_1(f-1)+1: \tilde{N}_1 f}). \quad (49)$$

We then have

$$\mathbf{X} = \mathcal{R}_d(\tilde{\mathbf{X}}). \quad (50)$$

In the noiseless case, the decoupled algorithm 2DMFDANM is proposed in the following theorem.

**Theorem 1:** If the true spatial angular frequencies  $\{\omega_{2i}\}_{i=1}^{K_2}$  can be correctly estimated from the signal  $\mathbf{Y}_2$  via the 1-D MMV-MFANM proposed in [33], then  $\|\tilde{\mathbf{Y}}\|_{\mathbb{A}}$  can be computed

by solving the following optimization problem:

$$\begin{aligned} \min_{\mathbf{T}_2, \tilde{\mathbf{T}}_1, \tilde{\mathbf{X}}} & \frac{1}{2\sqrt{\tilde{N}_1 \tilde{N}_2}} [\text{Tr}(\mathbf{T}_2) + \text{Tr}(\tilde{\mathbf{T}}_1)] \\ \text{s.t. } & \begin{bmatrix} \mathbf{T}_2 & \tilde{\mathbf{X}} \\ \tilde{\mathbf{X}}^H & \tilde{\mathbf{T}}_1 \end{bmatrix} \succcurlyeq 0 \\ & \mathbf{Y} = \mathcal{R}_d(\tilde{\mathbf{X}}) \end{aligned} \quad (51)$$

where  $\mathbf{Y} = [\mathbf{Y}^1, \dots, \mathbf{Y}^{N_f}]$ ,  $\mathbf{T}_2$  is an  $\tilde{N}_2 \times \tilde{N}_2$  Toeplitz matrix and  $\tilde{\mathbf{T}}_1$  is an  $N_f \times N_f$  block matrix with each block being a  $\tilde{N}_1 \times \tilde{N}_1$  Toeplitz matrix.

Theorem 1 is proved in the Appendix.

The spatial angular frequencies  $\omega_1$  and  $\omega_2$  can be extracted from  $\tilde{\mathbf{T}}_1$  and  $\mathbf{T}_2$ , respectively. To be specific,  $\mathbf{T}_2$  and  $\tilde{\mathbf{T}}_1$  are of rank  $K_2$  and  $K_1$ , respectively. The Vandermonde decomposition of  $\mathbf{T}_2$  corresponds to the spatial angular frequencies  $\{\omega_{2i}\}_{i=1}^{K_2}$ , and  $\tilde{\mathbf{T}}_1$  has the following structure:

$$\begin{aligned} \tilde{\mathbf{T}}_1 &= \sum_{i=1}^{K_1} c_i \cdot (\mathbf{p}_{\omega_i} \otimes \mathbf{z}_1(-\omega_{1i})) (\mathbf{p}_{\omega_i} \otimes \mathbf{z}_1(-\omega_{1i}))^H \\ &= \sum_{i=1}^{K_1} c_i \cdot (\mathbf{p}_{\omega_i} \mathbf{p}_{\omega_i}^H) \otimes (\mathbf{z}_1(-\omega_{1i}) \mathbf{z}_1(-\omega_{1i})^H). \end{aligned} \quad (52)$$

Define  $\mathbf{S}(\mathbf{T}_1)$  as

$$\mathbf{S}(\mathbf{T}_1) = \sum_{i=1}^{K_1} c_i \cdot (\mathbf{z}_1(-\omega_{1i}) \mathbf{z}_1(-\omega_{1i})^H) \otimes (\mathbf{p}_{\omega_i} \mathbf{p}_{\omega_i}^H) \quad (53)$$

we have

$$\mathbf{S}(\mathbf{T}_1) = \mathbf{P}^{\tilde{N}_1 N_f} \tilde{\mathbf{T}}_1 \mathbf{P}^{N_f \tilde{N}_1} \quad (54)$$

where  $\mathbf{P}^{mn} = \sum_{i=1}^n \sum_{j=1}^m (\mathbf{e}_j \otimes \mathbf{e}_i) (\mathbf{e}_i \otimes \mathbf{e}_j)^T$ . Note that  $\mathbf{S}(\mathbf{T}_1)$  is an  $\tilde{N}_1 \times \tilde{N}_1$  PSD block Toeplitz matrix with the rank of  $K_1$ , Lemma 2 in [31] guarantees that  $\mathbf{S}(\mathbf{T}_1)$  can be decomposed as (53), which corresponds to the spatial angular frequencies  $\{\omega_{1i}\}_{i=1}^{K_1}$ .

It is important to note that the hypothesis stated in theorem 1 is made only to facilitate the proof; numerical simulations show that (51) succeeds in correctly recovering the spatial angular frequencies even when the hypothesis is not satisfied.

In the case that noise is present, (51) is modified as

$$\begin{aligned} \min_{\mathbf{T}_2, \tilde{\mathbf{T}}_1, \tilde{\mathbf{X}}} & \frac{1}{2\sqrt{\tilde{N}_1 \tilde{N}_2}} [\text{Tr}(\mathbf{T}_2) + \text{Tr}(\tilde{\mathbf{T}}_1)] \\ \text{s.t. } & \begin{bmatrix} \mathbf{T}_2 & \tilde{\mathbf{X}} \\ \tilde{\mathbf{X}}^H & \tilde{\mathbf{T}}_1 \end{bmatrix} \succcurlyeq 0 \\ & \|\mathbf{Y} - \mathcal{R}_d(\tilde{\mathbf{X}})\|_2 \leq \epsilon. \end{aligned} \quad (55)$$

The complete decoupled algorithm 2DMFDANM is summarized in Algorithm 4. The P.S.D matrices in (51) and (55) are of size  $(N_f(N_2 - 1) + 1 + N_f^2(N_1 - 1) + N_f) \times (N_f(N_2 - 1) + 1 + N_f^2(N_1 - 1) + N_f)$  and contain  $O((N_f N_2 + N_f^2 N_1)^2)$  elements. Recall that the P.S.D matrices in (40) and (41) contain  $O((N_1 N_2 N_f^2)^2)$  elements, and it can be seen that the decoupled algorithm is much more computationally efficient than the original algorithm.

It is worth noting that the auxiliary problem (71) itself can also be viewed as a decoupled algorithm, whose scale

is smaller than that of (51). However, when the hypothesis in Theorem 1 is not satisfied, (71) may fail, while (51) still has the possibility of correctly estimating spatial angular frequencies because  $\tilde{p} \geq \hat{p}$ .

---

**Algorithm 2** MFPAiring
 

---

**Input:**  $\{\widehat{\omega}_{1i}\}_{i=1}^K$  and  $\{\widehat{\omega}_{2i}\}_{i=1}^K$ ,  $\{\mathbf{Y}^f\}_{f=1}^{N_f}$ ,  $N_1$ ,  $N_2$ ,  $N_f$ ,  $\epsilon$   
**Output:**  $\{\theta_i, \phi_i\}_{i=1}^K$   
 1 Solve (45) and obtain  $\tilde{\mathbf{S}}$ ;  
 2  $Nml = \sqrt{\text{diag}(\tilde{\mathbf{S}}^T \tilde{\mathbf{S}})}$ ;  
 3  $\tilde{\mathbf{S}}' \leftarrow \tilde{\mathbf{S}}/Nml$ ;  
 4  $\tilde{\mathbf{s}} \leftarrow \tilde{\mathbf{S}}' \cdot \mathbf{1}_{N_f}$ ;  
 5 Find the biggest  $K$  elements in  $\tilde{\mathbf{s}}$ , whose indices are denoted by  $idx$ ;  
 6 Pair the spatial angular frequencies  $\{\{\omega_{1i}, \omega_{2i}\}\}_{i=1}^K$  in accordance with  $idx$ ;  
 7  $\theta = \arcsin(\sqrt{\omega_1^2 + \omega_2^2} \cdot \frac{c}{f_{od}})$ ,  $\phi = \arctan(\frac{\omega_2}{\omega_1})$ ;

---



---

**Algorithm 3** Decoupled Algorithm via 2 1-D MMV-MF ANM
 

---

**Input:**  $\{\mathbf{Y}^f\}_{f=1}^{N_f}$ ,  $N_1$ ,  $N_2$ ,  $N_f$ ,  $\epsilon$   
**Output:**  $\{\theta_i, \phi_i\}_{i=1}^K$   
 1 Rearrange  $\{\mathbf{Y}^f\}_{f=1}^{N_f}$  into  $\mathbf{Y}_1$  and  $\mathbf{Y}_2$  according to (42);  
 2 Estimate  $\{\widehat{\omega}_{1i}\}_{i=1}^K$  and  $\{\widehat{\omega}_{2i}\}_{i=1}^K$  via 1-D MMV-MF ANM;  
 3  $\{\theta_i, \phi_i\}_{i=1}^K \leftarrow \text{Pairing}(\{\widehat{\omega}_{1i}\}_{i=1}^K, \{\widehat{\omega}_{2i}\}_{i=1}^K)$

---



---

**Algorithm 4** 2DMFDANM
 

---

**Input:**  $\{\mathbf{Y}^f\}_{f=1}^{N_f}$ ,  $N_1$ ,  $N_2$ ,  $N_f$ ,  $\epsilon$   
**Output:**  $\{\theta_i, \phi_i\}_{i=1}^K$   
 1  $\mathbf{Y} \leftarrow [\mathbf{Y}^1, \dots, \mathbf{Y}^{N_f}]$ ;  
 2 **for**  $k=1:2$  **do**  
 3    $\tilde{N}_k = N_f(N_k - 1) + 1$ ;  
 4 Construct mapping operator  $R_d$  in accordance with (49);  
 5 **if** noise-free **then**  
 6   Solve (51);  
 7 **else**  
 8   Solve (55);  
 9  $\{\omega_{2i}\}_{i=1}^K \leftarrow$  Vandermonde decomposition of  $T_2$ ;  
 10  $\mathbf{S}(T_1) = \mathbf{P}^{\tilde{N}_1 N_f} \tilde{\mathbf{T}}_1 \mathbf{P}^{N_f \tilde{N}_1}$ ;  
 11  $\{\omega_{1i}\}_{i=1}^K \leftarrow$  decompose  $\mathbf{S}(T_1)$  as (53);  
 12  $\{\theta_i, \phi_i\}_{i=1}^K \leftarrow \text{Pairing}(\{\widehat{\omega}_{1i}\}_{i=1}^K, \{\widehat{\omega}_{2i}\}_{i=1}^K)$

---

### C. Size-Reduced Algorithm—2DMFANM\_SizeRedu

As previously discussed in Section III-A, in (34), the algorithm's large scale is attributed to the sparsity of matrix  $\mathbf{H}$ . Consequently, the scale can be reduced by adjusting it. It should be noted that the introduction of the mapping operator  $\mathcal{R}$  is to write  $\Psi(\mathbf{Q}, \omega) \triangleq$

$[\mathbf{q}_1^H \tilde{\mathbf{a}}(1, \omega), \mathbf{q}_2^H \tilde{\mathbf{a}}(2, \omega), \dots, \mathbf{q}_{N_f}^H \tilde{\mathbf{a}}(N_f, \omega)]^T$  in the form of  $\Psi(\mathbf{Q}, \omega) = \mathbf{H}^H \mathbf{z}$  to induce a quadratic form. It is possible to achieve this objective with a much smaller mapping operator.

Let  $\mathcal{U}_r = \{[m_1, m_2] \cdot f \mid m_k \in 0, 1, \dots, N_k - 1, k = 1, 2, f \in 1, \dots, N_f\}$ . Let

$$\mathbf{z}_r(\omega) = \text{vec}(\mathbf{a}_{\mathcal{U}_{r2}}(\omega_2) \mathbf{a}_{\mathcal{U}_{r1}}(\omega_1)^T) \quad (56)$$

where  $\mathbf{a}_{\mathcal{U}_{rk}}(\omega_k) = [\mathbf{a}_k(\omega_k)]_{\mathcal{U}_{rk}}$ ,  $k = 1, 2$ . Let  $\mathbf{P}_k \in \mathbb{C}^{|\mathcal{U}_{rk}| \times \tilde{N}_k}$ ,  $k = 1, 2$ , where

$$[\mathbf{P}_k]_{i,j} = \begin{cases} 1, & j = \mathcal{U}_{rk}(i) + 1 \\ 0, & \text{otherwise.} \end{cases} \quad (57)$$

Thus, we have

$$\begin{aligned} \mathbf{z}_r(\omega) &= \mathbf{a}_{\mathcal{U}_{r1}}(\omega_1) \otimes \mathbf{a}_{\mathcal{U}_{r2}}(\omega_2) \\ &= (\mathbf{P}_1 \mathbf{z}_1(\omega_1)) \otimes (\mathbf{P}_2 \mathbf{z}_2(\omega_2)) \\ &= (\mathbf{P}_1 \otimes \mathbf{P}_2) \mathbf{z}. \end{aligned} \quad (58)$$

Based on (58), a new mapping operator  $\mathcal{R}_r$  can be defined. Let  $\mathbf{H}_r = \mathcal{R}_r^*(\mathbf{Q})$ , then we have

$$\begin{aligned} \Psi(\mathbf{Q}, \omega) &\triangleq [\mathbf{q}_1^H \tilde{\mathbf{a}}(1, \omega), \mathbf{q}_2^H \tilde{\mathbf{a}}(2, \omega), \dots, \mathbf{q}_{N_f}^H \tilde{\mathbf{a}}(N_f, \omega)]^T \\ &= \mathbf{H}_r^H \mathbf{z}_r(\omega). \end{aligned} \quad (59)$$

It can also be obtained that

$$\begin{aligned} \mathbf{z}_r(\omega) \mathbf{z}_r(\omega)^H &= (\mathbf{P}_1 \mathbf{z}_1 \mathbf{z}_1^H \mathbf{P}_1^H) \otimes (\mathbf{P}_2 \mathbf{z}_2 \mathbf{z}_2^H \mathbf{P}_2^H) \\ &= \left( \mathbf{P}_1 \left( \sum_{k_1=-\tilde{N}_1}^{\tilde{N}_1} \boldsymbol{\Theta}_{k_1} t_1^{-k_1} \right) \mathbf{P}_1^H \right) \\ &\quad \otimes \left( \mathbf{P}_2 \left( \sum_{k_2=-\tilde{N}_2}^{\tilde{N}_2} \boldsymbol{\Theta}_{k_2} t_2^{-k_2} \right) \mathbf{P}_2^H \right) \\ &= \sum_{k=-\tilde{N}}^{\tilde{N}} t^{-k} \boldsymbol{\Theta}_k^r \end{aligned} \quad (60)$$

where  $t_1 = \exp(j\omega_1)$ ,  $t_2 = \exp(j\omega_2)$ ,  $\boldsymbol{\Theta}_k = \boldsymbol{\Theta}_{k_1} \otimes \boldsymbol{\Theta}_{k_2}$ ,  $t^{-k} = t_1^{-k_1} t_2^{-k_2}$ . It yields  $\mathbf{z}_r^H \mathbf{P}_r \mathbf{z}_r = \text{Tr}(\mathbf{P}_r \mathbf{z}_r \mathbf{z}_r^H) = \sum_{k=-\tilde{N}}^{\tilde{N}} t^{-k} \text{Tr}(\boldsymbol{\Theta}_k^r \mathbf{P}_r)$ . As a result

$$\|\mathbf{Q}\|_{\mathbb{A}}^* \leq 1 \Leftrightarrow \begin{cases} \text{Tr}(\boldsymbol{\Theta}_k^r \mathbf{P}_r) = \delta_k, & k \in \mathcal{H} \\ \begin{bmatrix} \mathbf{P}_r & \mathbf{H}_r \\ \mathbf{H}_r^H & \mathbf{I}_{N_f} \end{bmatrix} \succcurlyeq 0 \\ \mathcal{R}_r(\mathbf{H}_r) = \mathbf{Q}. \end{cases} \quad (61)$$

As illustrated in (61), the dimensions of  $\mathbf{P}_r$  and  $\mathbf{H}_r$  are considerably smaller than those of  $\mathbf{P}_0$  and  $\mathbf{H}$ . This significantly reduces the scale of the problem. However, it is important to note that the right-hand side of (61) is more strict than  $\|\mathbf{Q}\|_{\mathbb{A}}^* \leq 1$ . This has a negative impact on the performance of the algorithm. In order to obtain a similar form of (40), it is necessary to use the dual matrix of  $\begin{bmatrix} \mathbf{P}_r & \mathbf{H}_r \\ \mathbf{H}_r^H & \mathbf{I}_{N_f} \end{bmatrix}$ . Compared to (40), the main difference is the dual of  $\mathbf{P}_r$ . The Lagrangian

dual associated with it is

$$\begin{aligned}
& \sum_{k_1=0}^{\tilde{N}_1} \sum_{k_2=-\tilde{N}_2}^{\tilde{N}_2} v_k \text{Tr}(\Theta_k^r P_r) \\
&= \sum_{k_1=0}^{\tilde{N}_1} \sum_{k_2=-\tilde{N}_2}^{\tilde{N}_2} v_k \text{Tr}(\Theta_k P_{\mathcal{U}}^H P_r P_{\mathcal{U}}) \\
&= \langle \text{Toep}_{2D}(\mathbf{v}), P_{\mathcal{U}}^H P_r P_{\mathcal{U}} \rangle_{\mathbb{R}} \\
&= \langle P_r, T(\mathbf{v}) \rangle_{\mathbb{R}}
\end{aligned} \tag{62}$$

where  $P_{\mathcal{U}} = P_1 \otimes P_2$ . Thus, the primal problem can be written as

$$\begin{aligned}
& \min_{\mathbf{W}, \mu, \tilde{\mathbf{X}}^{\star}} \frac{1}{2} [\text{Tr}(\mathbf{W}) + \text{Tr}(T(\mu))] \\
& \text{s.t.} \quad \begin{bmatrix} T(\mu) & \tilde{\mathbf{X}}^{\star} \\ \tilde{\mathbf{X}}^{\star H} & \mathbf{W} \end{bmatrix} \succcurlyeq 0 \\
& \quad \tilde{\mathbf{Y}} = \mathcal{R}_r(\tilde{\mathbf{X}}^{\star}) \\
& \quad T(\mu) = P_{\mathcal{U}} \text{Toep}_{2D}(\mu) P_{\mathcal{U}}^H
\end{aligned} \tag{63}$$

where  $\text{Toep}_{2D}(\mu)$  is a two-level Toeplitz matrix and  $\mu \in \mathbb{C}^{\tilde{N}_1 \times \tilde{N}_2}$ . When noise is present, the above optimization problem is modified as

$$\begin{aligned}
& \min_{\mathbf{W}, \mu, \tilde{\mathbf{X}}^{\star}} \frac{1}{2} [\text{Tr}(\mathbf{W}) + \text{Tr}(T(\mu))] \\
& \text{s.t.} \quad \begin{bmatrix} T(\mu) & \tilde{\mathbf{X}}^{\star} \\ \tilde{\mathbf{X}}^{\star H} & \mathbf{W} \end{bmatrix} \succcurlyeq 0 \\
& \quad \|\tilde{\mathbf{Y}} - \mathcal{R}_r(\tilde{\mathbf{X}}^{\star})\| \leq \epsilon \\
& \quad T(\mu) = P_{\mathcal{U}} \text{Toep}_{2D}(\mu) P_{\mathcal{U}}^H.
\end{aligned} \tag{64}$$

The complete algorithm is summarized in Algorithm 5.

The existence of  $P_{\mathcal{U}}$  has the effect of reducing the scale of the problem. This reduction in scale can also be applied to the aforementioned decoupled algorithms. With regard to Algorithm (51), the key is to remove the all-zero rows or columns in  $\mathcal{R}_d^*(\mathbf{X})$ . The case of removing all-zero columns has already been discussed in (71) in the Appendix. With regard to the removal of all-zero rows, it is possible to simply modify the matrix  $T_2$  to  $T_{2\text{new}} = P_2 T_2 P_2^H$  and adjust the mapping operator in accordance with this change.

#### IV. SIMULATION RESULTS

##### A. Simulations of the 2DMFANM Algorithm

In this study, we have conducted a series of numerical simulations to assess the efficacy of the proposed algorithms.

Consider the case of three wideband far-field waves impinging on a  $5 \times 5$  URA. The azimuth and elevation angles are set to values of  $(-60^\circ, -45^\circ, -30^\circ)$  and  $(30^\circ, 40^\circ, 45^\circ)$ , respectively. It is assumed that the wave velocity is equal to  $v = 1500$  m/s. The source signals are described by the multifrequency model with a base frequency of  $f_0 = 1000$  Hz. The distance between the elements of the array is equal to half of the maximum wavelength,  $d = v/2f_0$ . The source signals, as defined in (1), are presumed to be independent and synthesized from a complex normal distribution  $\mathcal{CN}(0, I_{N_f})$ . The noise is modeled as white Gaussian noise. The optimization

##### Algorithm 5 2DMFANM\_SizeRedu

---

**Input:**  $\{Y^f\}_{f=1}^{N_f}$ ,  $N_1$ ,  $N_2$ ,  $N_f$ ,  $\epsilon$   
**Output:**  $\{\{\theta_i, \phi_i\}\}_{i=1}^K$

- 1  $\tilde{\mathbf{Y}} \leftarrow [\text{vec}(Y^1), \dots, \text{vec}(Y^{N_f})];$
- 2 **for**  $k=1:2$  **do**
- 3    $\tilde{N}_k = N_f(N_k - 1) + 1;$
- 4 Construct the mapping operator  $R_r;$
- 5 Compute  $P_1$  and  $P_2$  in accordance with (57);
- 6  $P_{\mathcal{U}} \leftarrow P_1 \otimes P_2;$
- 7 **if** noise-free **then**
- 8   Solve (63);
- 9 **else**
- 10   Solve (64);
- 11  $\{\{\omega_{1i}, \omega_{2i}\}\}_{i=1}^K \leftarrow \text{MaPP}(\text{Toep}_{2D}(\mu));$
- 12  $\theta = \arcsin(\sqrt{\omega_1^2 + \omega_2^2 \cdot \frac{c}{f_0 d}}), \phi = \arctan(\frac{\omega_2}{\omega_1})$

---

problems in the algorithms are solved using CVX [37]. The simulations are performed on a computer with 2 Intel<sup>1</sup> Xeon<sup>1</sup> Gold 6455 B at 3.00 GHz using MATLAB R2022b. Subsequent results are derived from 100 Monte Carlo simulation trials.

Since there are few studies on wideband 2-D DOA estimation methods for small sample size scenarios similar to the one considered in this article, in order to demonstrate the superior performance of the proposed method, we generalize the existing state-of-the-art methods to wideband 2-D scenarios and compare them with the proposed method. The proposed method is compared with the ISSM [7] algorithm and the SBL-based algorithm [38]. Specifically, to utilize the ISSM in small-sample scenarios, the ANM method is employed to estimate the covariance matrices corresponding to different subbands, and subsequently, the ISSM method is applied to estimate the desired angles from these covariance matrices. This algorithm is referred to as ANM-ISSM.

In the 2DMFANM algorithm, the value of  $N_f$  is set to 5. In the absence of noise, the estimation outcomes are depicted in Fig. 2. Fig. 2(a)–(c) compares 2DMFANM with the SBL-based algorithm and the ANM-ISSM approach in estimating spatial angular frequencies. Fig. 2(d)–(f) compares the elevation and azimuth angles estimated by the three algorithms. Fig. 2 reveals that by jointly harnessing the additional data from multiple frequencies, both our 2DMFANM and the SBL-based approach yield estimations that cluster tightly around the actual values, whereas the ANM-ISSM method fails to produce accurate results owing to aliasing. Moreover, the 2DMFANM method yields a tighter cluster than the SBL-based approach, thereby demonstrating the superior performance of the proposed method.

##### B. Simulations of the Decoupled and Size-Reduced Algorithms

This section is dedicated to demonstrating the effectiveness of the proposed fast algorithms. Prior to presenting the

<sup>1</sup>Registered trademark.



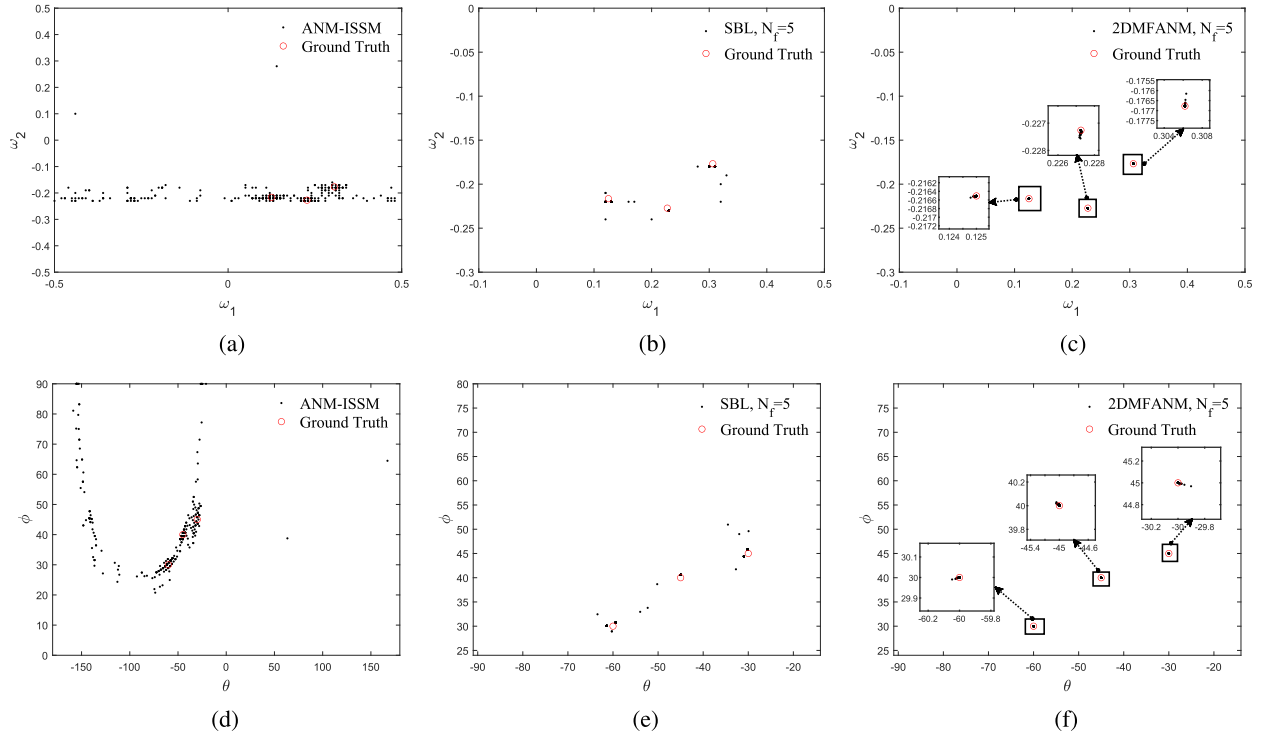


Fig. 2. Estimations of spatial angular frequencies and elevation and azimuth angles under the noiseless condition. (a) Spatial angular frequencies estimation by ANM-ISSM. (b) Spatial angular frequencies estimation by SBL. (c) Spatial angular frequencies estimation by 2DMFANM. (d) Elevation and azimuth angles estimation by ANM-ISSM. (e) Elevation and azimuth angles estimation by SBL. (f) Elevation and azimuth angles estimation by 2DMFANM.

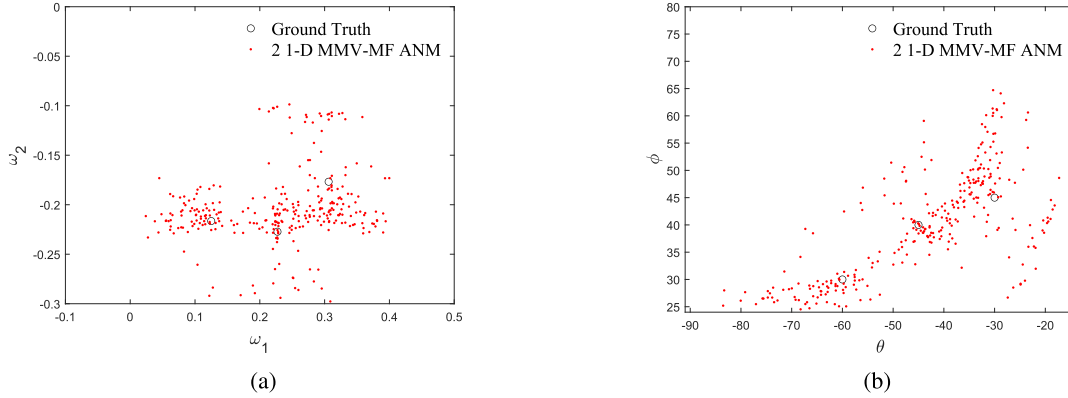


Fig. 3. Estimation results of Algorithm 3. (a) Spatial angular frequencies estimation. (b) Elevation and azimuth angles estimation.

simulation results of the proposed fast algorithms, it is first necessary to demonstrate that Algorithm 3, which employs two 1-D MMV-MF ANM algorithms, is unsuitable for the 2-D case. Fig. 3 illustrates the estimation outcomes of Algorithm 3 in the noise-free case when  $N_f$  is set to 5. It becomes evident that the algorithm is unable to accurately estimate the true values and therefore cannot be considered a valid decoupled approach.

As previously stated in the final paragraph of Section III-C, size-reducing methods can also be applied to the decoupled algorithm. By removing the all-zero columns and rows, the sizes of  $\tilde{T}_1$  and  $T_2$  in (51) are significantly reduced. For the sake of clarity, we refer to the algorithms that reduce the size of  $\tilde{T}_1$  and  $T_2$  as 2DMFDANM

\_SizeRedu11 and 2DMFDANM\_SizeRedu12, respectively. When both the sizes of  $\tilde{T}_1$  and  $T_2$  are reduced, the algorithm is called 2DMFDANM\_SizeRedu2. It is important to note that the algorithms 2DMFDANM\_SizeRedu11 and 2DMFDANM\_SizeRedu12 cannot be considered symmetrical, as the information contained in  $T_2$  is distinct from that of  $\tilde{T}_1$ . While  $T_2$  comprises only the DOA data, the frequency information is also coupled in  $\tilde{T}_1$ .

Fig. 4 illustrates the estimation outcomes of the original and fast algorithms in the noiseless case when  $N_f$  is set to 5. It can be seen that the size-reduced algorithm 2DMFANM\_SizeRedu achieves an estimation accuracy similar to that of the original algorithm, while the decoupled algorithms can produce spurious estimations. The deterioration is more significant in

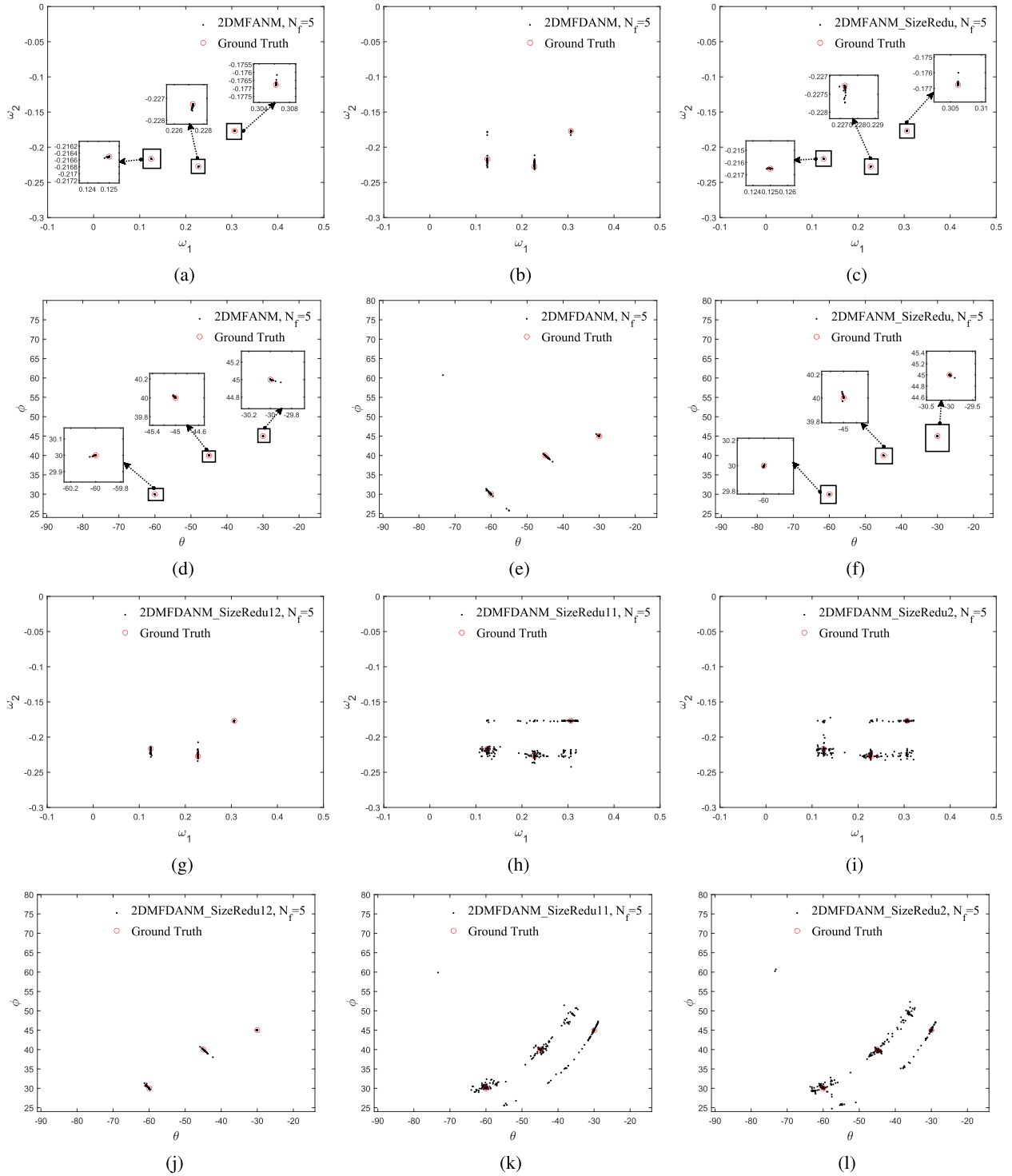


Fig. 4. Estimation results of fast algorithms. (a) Spatial angular frequencies estimation by 2DMFANM. (b) Spatial angular frequencies estimation by 2DMFDANM. (c) Spatial angular frequencies estimation by 2DMFANM\_SizeRedu. (d) Elevation and azimuth angles estimation by 2DMFANM. (e) Elevation and azimuth angles estimation by 2DMFDANM. (f) Elevation and azimuth angles estimation by 2DMFANM\_SizeRedu. (g) Spatial angular frequencies estimation by 2DMFDANM\_SizeRedu12. (h) Spatial angular frequencies estimation by 2DMFDANM\_SizeRedu11. (i) Spatial angular frequencies estimation by 2DMFDANM\_SizeRedu1. (j) Elevation and azimuth angles estimation by 2DMFDANM\_SizeRedu12. (k) Elevation and azimuth angles estimation by 2DMFDANM\_SizeRedu11. (l) Elevation and azimuth angles estimation by 2DMFDANM\_SizeRedu2.

size-reduced decoupled algorithms 2DMFDANM\_SizeRedu11 and 2DMFDANM\_SizeRedu2.

The running time of the fast algorithms with  $N_f$  ranging from 1 to 5 is presented in Table I. It can be observed that the running time of the original algorithm increases

dramatically with  $N_f$ , demonstrating the necessity of fast algorithms. Both the decoupled algorithm and size-reduced algorithm demonstrate the capacity to reduce the running time, with the decoupled algorithm exhibiting a more pronounced reduction. In comparison to other size-reducing schemes,

TABLE I  
RUNNING TIME/s

Method	$N_f$				
	1	2	3	4	5
2DMFANM	0.4608	2.4002	13.3764	150.2877	863.6651
2DMFDANM	0.7958	0.9415	6.0580	8.3916	31.8204
2DMFANM_SizeRedu	0.4330	0.8744	2.7444	9.0755	71.1213
2DMFDANM_SizeRedu12	0.6627	0.8482	1.3451	4.8456	21.6289
2DMFDANM_SizeRedu11	0.6673	0.7560	0.8253	1.0317	1.3889
2DMFDANM_SizeRedu2	0.6618	0.7331	0.7553	0.8845	1.0855

2DMFDANM\_SizeRedu12, which solely reduces the size of  $T_2$ , only marginally enhances speed. Nevertheless, despite the fact that the other two algorithms achieve the fastest speed, their estimation accuracy is too low to be accepted in practical scenarios, as shown in Fig. 4.

In order to further analyze the estimation accuracy of the fast algorithms, we define the root square error (RSE) of the spatial angular frequencies to determine whether an estimation is successful. The RSE for the  $k$ th target in the  $n$ th trial is defined as  $\text{RSE}_{\omega_{k,n}} = (((\omega_{1k} - \hat{\omega}_{1k,n})^2 + (\omega_{2k} - \hat{\omega}_{2k,n})^2))^{1/2}$ , where  $\omega_k = [\omega_{1k}, \omega_{2k}]^T$  is the true spatial angular frequency of the  $k$ th target, and  $\hat{\omega}_{k,n} = [\hat{\omega}_{1k,n}, \hat{\omega}_{2k,n}]^T$  is the estimated spatial angular frequency for the  $k$ th target in the  $n$ th trial. Inspection of Fig. 4(b), (e), (g), and (j) reveals that although a few isolated spurious estimations exist, the majority of the estimations cluster tightly around the true values. To demonstrate this property, spurious estimations are excluded from the computation of the RSE. Here, a trial is considered to be successful if the RSE is not greater than 0.05. The RSE can be understood as the Euclidean distance between the estimated and true values. The definition of successful estimations in this article is similar to that presented in [39]. In [39], the success of estimation is defined as the case where the true DOA values are included in the estimated bins. According to the definition of successful estimation in this study, the bins in [39] can be interpreted as the circular region centered at the estimated values.

The root-mean-square error (RMSE) is used to evaluate the accuracy of the estimations. The RMSE of the spatial angular frequency and the elevation and azimuth angles are defined as

$$\text{RMSE}_{\omega} = \left( \frac{1}{KN} \sum_{n=1}^N \sum_{k=1}^K ((\omega_{1k} - \hat{\omega}_{1k,n})^2 + (\omega_{2k} - \hat{\omega}_{2k,n})^2) \right)^{\frac{1}{2}}$$

and

$$\text{RMSE}_{\theta, \phi} = \left( \frac{1}{KN} \sum_{n=1}^N \sum_{k=1}^K ((\theta_k - \hat{\theta}_{k,n})^2 + (\phi_k - \hat{\phi}_{k,n})^2) \right)^{\frac{1}{2}}$$

respectively, where  $N$  is the number of trials,  $\theta_k$  and  $\phi_k$  are the true elevation and azimuth angles of the  $k$ th target, and  $\hat{\theta}_{k,n}$  and  $\hat{\phi}_{k,n}$  are the estimated elevation and azimuth angles for the  $k$ th target in the  $n$ th trial.

The number of successful trials is summarized in Table II, and the RMSEs of the spatial angular frequencies and azimuth and elevation angles are listed in Tables III and IV. As can be seen from Table II, the success rates of 2DMFDANM, 2DMFDANM\_SizeRedu and 2DMFDANM\_SizeRedu12 are

TABLE II  
NUMBER OF SUCCESSFUL TRIALS (TOTAL TRIALS: 100)

Method	$N_f$				
	1	2	3	4	5
2DMFANM	71	100	100	100	100
2DMFDANM	68	72	92	96	97
2DMFANM_SizeRedu	64	98	100	100	100
2DMFDANM_SizeRedu12	60	86	86	94	95
2DMFDANM_SizeRedu11	44	58	58	49	49
2DMFDANM_SizeRedu2	40	57	57	46	38

significantly improved with the increment of  $N_f$ , while the performance of the other size-reduced decoupled algorithms is not improved markedly with increasing  $N_f$ . The diminished performance of these size-reduced decoupled algorithms (2DMFDANM\_SizeRedu11 and 2DMFDANM\_SizeRedu2) indicates that although the decoupled algorithm can be significantly accelerated by reducing the size of  $\tilde{T}_1$ , the estimation accuracy is significantly degraded because of the destruction of the structure of  $\tilde{T}_1$ . It is therefore recommended that these two algorithms should not be used in practical scenarios where the estimations are required to be accurate.

An inspection of Tables III and IV reveals that although the original algorithm 2DMFANM achieves the highest estimation accuracy, its computational demands increase dramatically with  $N_f$ . The size-reduced algorithm 2DMFANM\_SizeRedu achieves an estimation accuracy similar to that of 2DMFANM while greatly reducing the running time. However, when  $N_f$  is relatively high, the computational burden remains challenging. The decoupled algorithm 2DMFDANM achieves the fastest running speed, but its estimation accuracy is degraded. It can be concluded that in practical scenarios where computational resources are sufficient, 2DMFANM\_SizeRedu is the preferred option as it can yield accurate estimations. Conversely, in scenarios where computational resources are limited, 2DMFDANM can greatly reduce the running time at the expense of sacrificing some accuracy.

### C. Estimation Performance in Noisy Environments

In this section, the aforementioned methods are subjected to further comparisons under noisy conditions. The simulation setup is the same as in the simulation in Section IV-A. We validate the performance of the proposed 2DMFANM, the SBL, the ANM-ISSM, the proposed 2DMFDANM, and the proposed 2DMFANM\_SizeRedu. A trial is deemed successful when the RSE of the spatial angular frequency is less than 0.2. We only consider successful trials when calculating the RMSE of the algorithms' outcomes in order to make the calculation more reasonable. The change curves of the number

TABLE III  
RMSE OF ELEVATION AND AZIMUTH ANGLES

Method	$N_f$				
	1	2	3	4	5
<b>2DMFANM</b>	0.0431	$3.4171 \times 10^{-8}$	$1.9641 \times 10^{-8}$	$1.18 \times 10^{-8}$	$2.2345 \times 10^{-9}$
<b>2DMFDANM</b>	6.1195	2.8204	5.2857	3.5938	2.9025
<b>2DMFANM_SizeRedu</b>	0.4861	0.7944	$1.0884 \times 10^{-8}$	$3.0678 \times 10^{-9}$	$1.0003 \times 10^{-9}$
<b>2DMFDANM_SizeRedu12</b>	3.4289	5.1461	4.2065	6.7603	2.8091
<b>2DMFDANM_SizeRedu11</b>	1.7158	4.1229	3.9118	4.5334	2.6232
<b>2DMFDANM_SizeRedu2</b>	2.4921	6.1523	4.3622	4.4866	4.6134

TABLE IV  
RMSE OF SPATIAL ANGULAR FREQUENCY

Method	$N_f$				
	1	2	3	4	5
<b>2DMFANM</b>	0.0277	0.0076	$8.1759 \times 10^{-4}$	$1.7506 \times 10^{-4}$	$6.2904 \times 10^{-5}$
<b>2DMFDANM</b>	0.0322	0.0158	0.0044	0.0029	0.0025
<b>2DMFANM_SizeRedu</b>	0.0232	0.0112	0.0024	$2.1556 \times 10^{-4}$	$8.1636 \times 10^{-5}$
<b>2DMFDANM_SizeRedu12</b>	0.0298	0.0050	0.0050	0.0056	0.0054
<b>2DMFDANM_SizeRedu11</b>	0.0323	0.0248	0.0248	0.0239	0.0270
<b>2DMFDANM_SizeRedu2</b>	0.0352	0.0279	0.0279	0.0258	0.0227

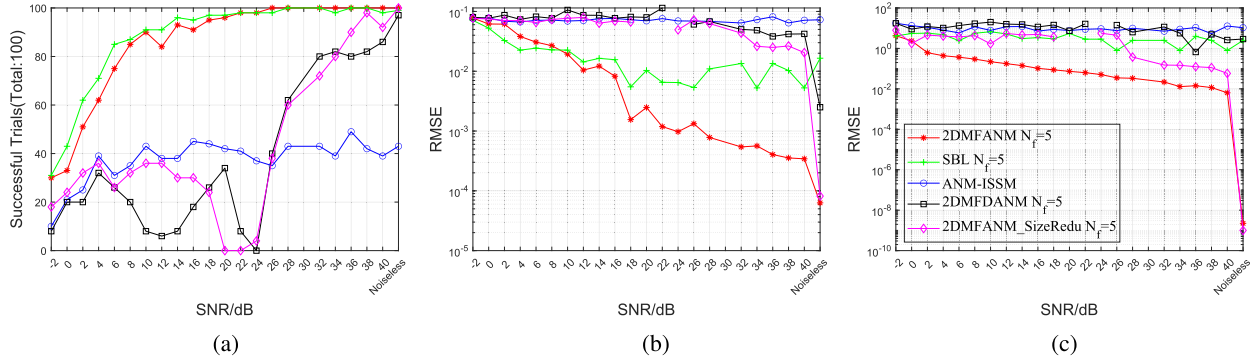


Fig. 5. RMSE and the number of successful trials versus SNR. (a) Number of successful trials (total trials: 100). (b) RMSE of estimations for spatial angular frequencies. (c) RMSE of estimations for elevation and azimuth angles.

of successful trials, the RMSE of spatial angular frequencies, and the RMSE of elevation and azimuth angles with SNR ranging from  $-2$  to  $40$  dB are plotted in Fig. 5(a)–(c), respectively.

From Fig. 5(a), it can be seen that the number of successful trials shows an increasing trend as the SNR increases for all methods. In comparison to the ANM-ISSM approach, our 2DMFANM method demonstrated a higher successful rate under low SNR conditions, indicating that our method can take full advantage of information from multiple frequencies to enhance performance while suppressing aliasing. Although the proposed fast algorithms significantly reduce the computation time, they adversely affect their robustness to noise and estimation accuracy. When the SNR is below  $24$  dB, the fast algorithms exhibit limitations in providing accurate estimations. However, when the SNR exceeds  $30$  dB, the success rates of the proposed fast algorithms are substantially higher than those of the ANM-ISSM algorithm, achieving an acceptable estimation success rate.

As evidenced by Fig. 5(b) and (c), the performance of all the methods exhibit an improvement as the SNR increases, with our 2DMFANM method exhibiting a more pronounced enhancement.

It is noteworthy that the results shown in Fig. 5(b) and (c) are not completely matched. It can be observed in Fig. 5(b) that the proposed 2DMFANM method does not significantly improve the performance compared with SBL when the SNR is low. However, as illustrated in Fig. 5(c), the performance of 2DMFANM is significantly better than that of SBL in this case. Fig. 5(b) demonstrates that the proposed fast algorithms do not perform as effectively as the SBL algorithm in estimating the spatial angular frequencies even when the SNRs are higher than  $30$  dB. However, Fig. 5(c) illustrates that in these cases, the performance of 2DMFANM\_SizeRedu in estimating the elevation and azimuth angles significantly surpasses that of the SBL algorithm, while the performance of 2DMFDANM approximates that of the SBL algorithm. This is primarily due to the nonlinear relationship between the elevation and azimuth angles ( $\theta$ ,  $\phi$ ) and the spatial angular frequency components ( $f_1$ ,  $f_2$ ). As a result, a lower RMSE for the spatial angular frequencies can result in a larger RMSE of the azimuth and elevation angles. The on-grid nature of the SBL results in estimation outcomes that fall on fixed grids, with some even falling on the same grids. In contrast, the gridless property of the proposed algorithm enables it to yield estimations that cluster continuously around true values. Consequently, when



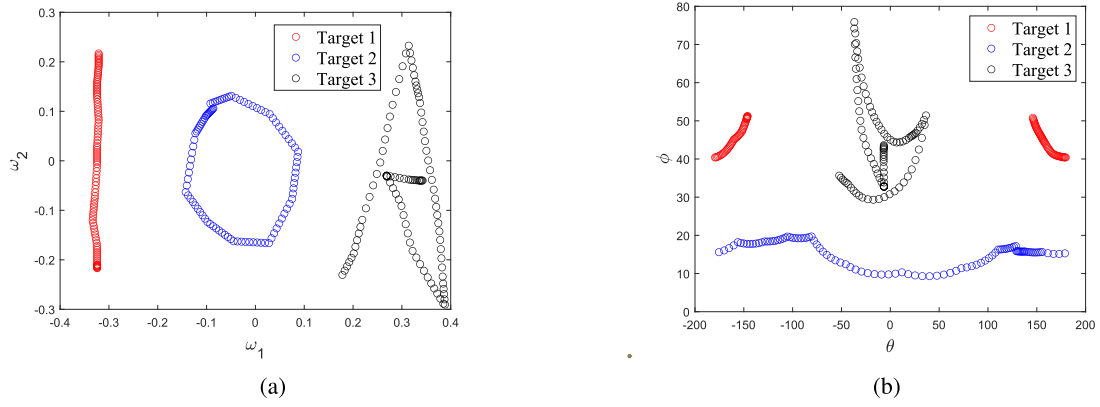


Fig. 6. Spatial angular frequencies and elevation and azimuth angles of targets when the array is moving. (a) Spatial angular frequencies. (b) Elevation and azimuth angles.

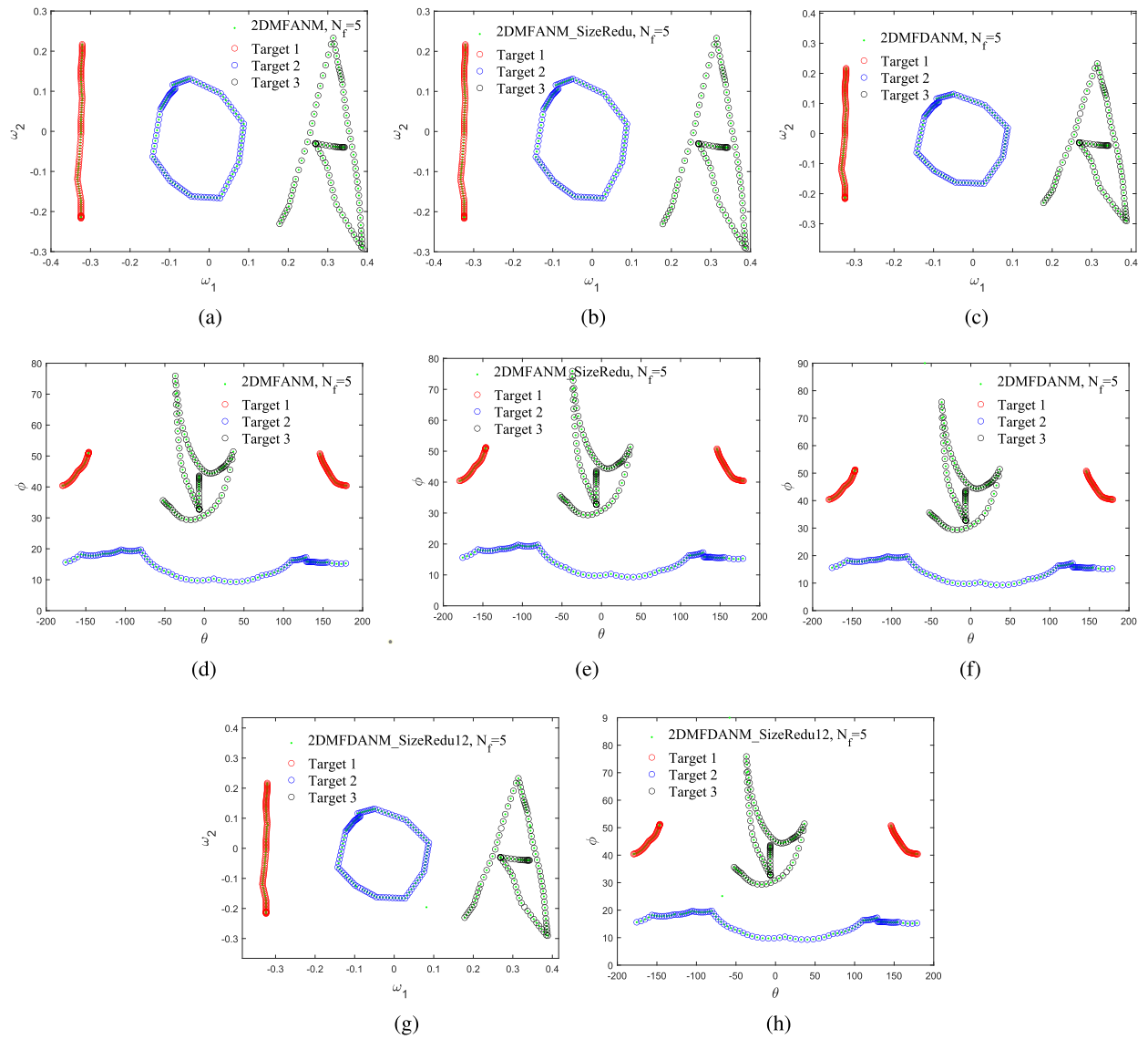


Fig. 7. Estimations of spatial angular frequencies and elevation and azimuth angles when the array is moving. (a) Spatial angular frequencies estimation by 2DMFANM. (b) Spatial angular frequencies estimation by 2DMFANM\_SizeRedu. (c) Spatial angular frequencies estimation by 2DMFDANM. (d) Elevation and azimuth angles estimation by 2DMFANM. (e) Elevation and azimuth angles estimation by 2DMFANM\_SizeRedu. (f) Elevation and azimuth angles estimation by 2DMFDANM. (g) Spatial angular frequencies estimation by 2DMFDANM\_SizeRedu12. (h) Elevation and azimuth angles estimation by 2DMFDANM\_SizeRedu12.

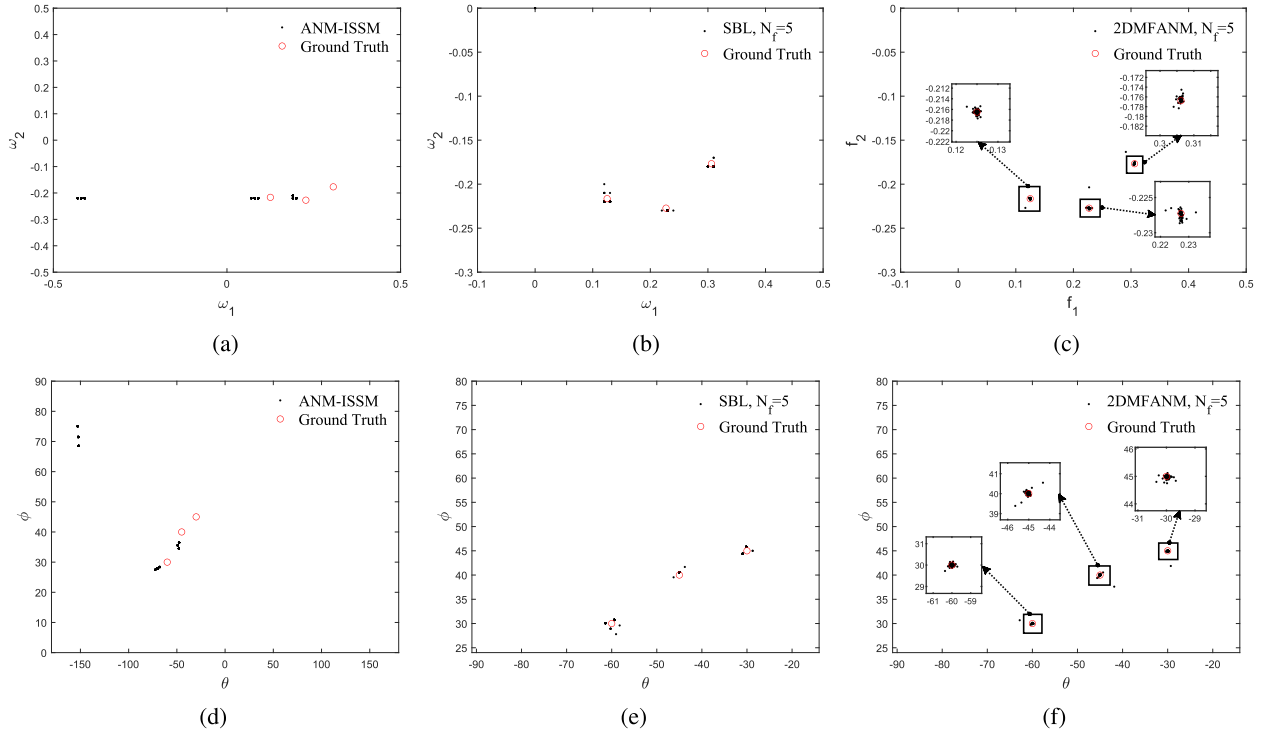


Fig. 8. Estimations of spatial angular frequencies and elevation and azimuth angles when SNR = 22 dB. (a) Spatial angular frequencies estimation by ANM-ISSM. (b) Spatial angular frequencies estimation by SBL. (c) Spatial angular frequencies estimation by 2DMFANM. (d) Elevation and azimuth angles estimation by ANM-ISSM. (e) Elevation and azimuth angles estimation by SBL. (f) Elevation and azimuth angles estimation by 2DMFANM.

the spatial angular frequencies are converted into elevation and azimuth angles, our gridless methods are likely to provide more accurate estimations. The advantage of the gridless property can be further illustrated by examining the cases when the SNR is high. When the SNR exceeds 20 dB, our 2DMFANM method outperforms SBL to a significant extent, especially in the noise-free case. When noise is not present, both fast algorithms 2DMFDANM and 2DMFANM\_SizeRedu outperform the SBL method.

#### D. Performance of the Proposed Algorithm With Varying Elevation and Azimuth Angles Due to Array Movement

To assess the efficacy of the proposed algorithms when the elevation and azimuth angles change as the array moves, we selected 100 consecutive sets of target angles to simulate the change in the target angles when the array moves and estimated them using the proposed algorithms. The spatial angular frequencies and the elevation and azimuth angles of the targets are depicted in Fig. 6.

Because 2DMFDANM\_SizeRedu11 and 2DMFDANM\_SizeRedu2 will provide incorrect estimations, here we only test other algorithms. The estimated outcomes in the absence of noise are shown in Fig. 7. As shown in Fig. 7, the proposed algorithms can all achieve accurate estimations when the array is moving.

### V. EXPERIMENTAL DATA ANALYSIS

In this section, we use experimental data to verify the effectiveness of the proposed method.

Data are obtained from the ShipsEar [40] dataset. In this study, we use the noise radiated by the passenger ship Mar de Cangas when it was entering (ID: 06), the noise generated by the ocean liner Adventure of the seas when it was maneuvering (ID: 22), and the sound generated by it when it was slowing (ID: 24) as the signal sources. The signals received by each array element can be obtained by delaying the signals by the corresponding delay time. It is noteworthy that this operation is frequently employed in scenarios where single-channel signals are utilized to simulate array signals. Specifically, in [41], Scheibler et al. [42] synthesized single-channel signals into multichannel signals using the Pyroomacoustics package, which accounts for the effect of reflected waves. These waves are equated to image sources using the image source model and are delayed appropriately and summed to obtain the array received signal. In this study, we do not consider the effect of reflected waves (which is beyond the scope of this article); therefore, we solely delay and sum the target signals. Natural ambient noises are also added to the target signals to verify the effectiveness of the proposed method in real-world scenarios. In this article, the noises added are from the recording Maximum Flow (ID: 81). This recording recorded the noise of the flow when the flow was 6.4 cm/s and the wind speed was 5.29 km/h. The settings of the target signals and the array are the same as before, except that the base frequency is changed to  $f_0 = 100$  Hz. The receiving array is a  $5 \times 5$  URA with an array element spacing of half the maximum wavelength, which is  $d = v/(2f_0)$ . The wave velocity is equal to  $v = 1500$  m/s. The azimuth and elevation angles of the targets are  $(-60^\circ, -45^\circ, -30^\circ)$  and  $(30^\circ, 40^\circ, 45^\circ)$ , respectively. The signal-to-noise ratio can be adjusted by

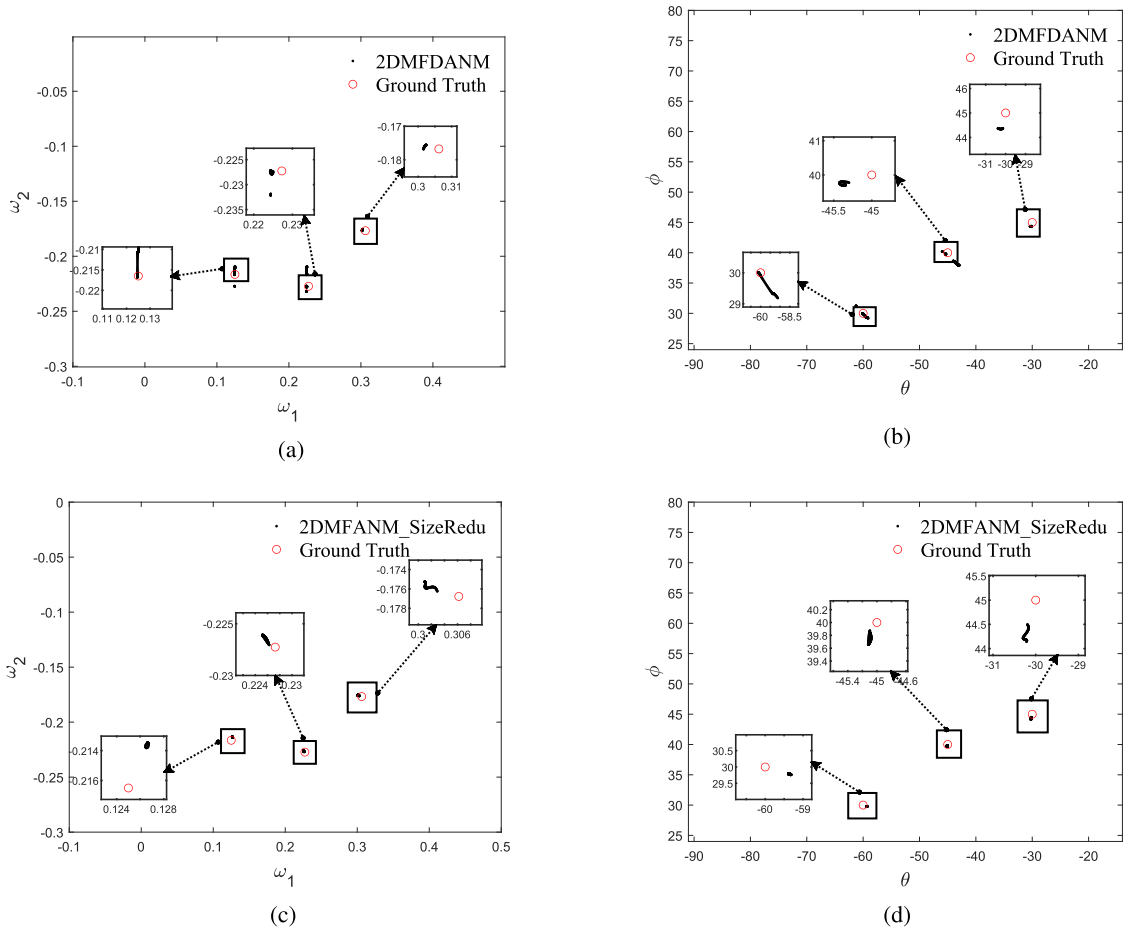


Fig. 9. Estimations of spatial angular frequencies and elevation and azimuth angles when SNR = 35 dB. (a) Spatial angular frequencies estimation by 2DMFDANM. (b) Elevation and azimuth angles estimation by 2DMFDANM. (c) Spatial angular frequencies estimation by 2DMFANM\_SizeRedu. (d) Elevation and azimuth angles estimation by 2DMFANM\_SizeRedu.

modifying the amplitude of the target signals and the noise.

Signals received by the array are first filtered through an FIR low-pass filter with a cut-off frequency of 600 Hz. The signals are then transformed into the multifrequency form after being filtered through five bandpass filters, with the central frequency of each filter being 100, 200, 300, 400, and 500 Hz. We select 100 consecutive output data points to test the performance of the proposed algorithms. We first compare the 2DMFANM algorithm with the SBL-based algorithm and the ANM-ISSM methods. In this experiment, the SNR is set to 22 dB. At this SNR, the proposed 2DMFANM significantly outperforms both the SBL and ANM-ISSM algorithms, as shown in Fig. 5(b). The estimation outcomes are depicted in Fig. 8.

As shown in Fig. 8, the estimation results of each algorithm are consistent with the simulation results, which shows that the 2DMFANM algorithm is applicable to practical scenarios and outperforms the state-of-the-art methods.

As shown in Fig. 5, although the proposed fast algorithms 2DMFDANM and 2DMFANM\_SizeRedu can significantly reduce the computational burden, this comes at the cost of some loss in accuracy. However, when the SNR exceeds 35 dB, these methods can also provide accurate estimations. By setting the SNR to 35 dB, the estimation results of the

fast algorithms are illustrated in Fig. 9. As can be seen in Fig. 9, the proposed fast algorithms can achieve acceptable estimations with experimental data, demonstrating their ability for real-world applications.

## VI. CONCLUSION

In this study, we have proposed a novel 2DMFANM algorithm for wideband joint elevation-azimuth angle estimation. The algorithm addresses grid mismatch issues by employing the gridless approach ANM and leverages the additional information inherent in wideband signals via the multifrequency model. Compared with the SBL-based algorithm and ISSM approach, numerical simulations and experimental data analysis demonstrate the superior performance of the proposed method. As the original 2DMFANM algorithm is computationally demanding, two fast algorithms have been derived. In particular, 2DMFDANM decouples 2-D information, while 2DMFANM\_SizeRedu removes redundant information. Theoretical and numerical analyses have demonstrated that these algorithms significantly reduce the size of the problem with only minor losses in estimation accuracy.

Through numerical simulations and analysis of experimental data, this research has shown that the ANM technique can be effectively utilized for high-precision, wideband 2-D DOA

estimation problems. However, it is important to note that the theoretical performance guarantee of the proposed methods has not been established within this article. Further studies are required to better understand the mathematical mechanisms underlying the superb performance of the proposed algorithms.

#### APPENDIX PROOF OF THEOREM 1

*Proof of Theorem 1:* Let the optimal solution to (51) be  $\tilde{p}$ . We first prove  $\|\tilde{\mathbf{Y}}\|_{\mathbb{A}} \geq \tilde{p}$ . Let the atomic decomposition be  $\tilde{\mathbf{Y}} = \sum_{i=1}^r c_i \tilde{\mathbf{A}}(\omega_i) \odot \mathbf{p}_{\omega_i}^T$ . Then, a feasible solution to (51) can be constructed as

$$\begin{aligned} \mathbf{T}_2 &= \sum_{i=1}^K |c_{2i}|^2 \mathbf{z}_2(\omega_{2i}) \mathbf{z}_2(\omega_{2i})^H \\ \tilde{\mathbf{T}}_1 &= \sum_{i=1}^K |c_{1i}|^2 (\mathbf{p}_{\omega_i}^* \otimes \mathbf{z}_1(-\omega_{1i})) (\mathbf{p}_{\omega_i}^* \otimes \mathbf{z}_1(-\omega_{1i}))^H \\ \tilde{\mathbf{X}} &= \sum_{i=1}^K c_{2i} c_{1i}^* \mathbf{z}_2(\omega_{2i}) \mathbf{p}_{\omega_i}^T \otimes \mathbf{z}_1(-\omega_{1i})^H \end{aligned} \quad (65)$$

where  $c_{1i} = \sqrt{|c_i|} \cdot (\tilde{N}_2/\tilde{N}_1)^{1/4}$ ,  $c_{2i} = \sqrt{|c_i|} \cdot \text{sign}(c_i) \cdot (\tilde{N}_1/\tilde{N}_2)^{1/4}$ . It is easy to verify that  $\mathbf{Y} = \mathcal{R}_d(\tilde{\mathbf{X}})$  and

$$\begin{bmatrix} \mathbf{T}_2 & \tilde{\mathbf{X}} \\ \tilde{\mathbf{X}}^H & \tilde{\mathbf{T}}_1 \end{bmatrix} = \sum_{i=1}^K \begin{bmatrix} c_{2i} \mathbf{z}_2(\omega_{2i}) \\ c_{1i} \mathbf{p}_{\omega_i}^* \otimes \mathbf{z}_1(-\omega_{1i}) \end{bmatrix} \cdot \begin{bmatrix} c_{2i} \mathbf{z}_2(\omega_{2i}) \\ c_{1i} \mathbf{p}_{\omega_i}^* \otimes \mathbf{z}_1(-\omega_{1i}) \end{bmatrix}^H \succcurlyeq 0. \quad (66)$$

It is obvious that  $\text{Tr}(\mathbf{T}_2) = \sum_{i=1}^K |c_{2i}|^2 \tilde{N}_2 = \sum_{i=1}^K |c_i| \sqrt{\tilde{N}_1 \tilde{N}_2}$ , and

$$\begin{aligned} \text{Tr}(\tilde{\mathbf{T}}_1) &= \sum_{i=1}^K |c_i| \sqrt{\tilde{N}_2/\tilde{N}_1} \text{Tr}((\mathbf{p}_{\omega_i}^* \otimes \mathbf{z}_1)(\mathbf{p}_{\omega_i}^* \otimes \mathbf{z}_1^H)) \\ &= \sum_{i=1}^K |c_i| \sqrt{\tilde{N}_1 \tilde{N}_2}. \end{aligned} \quad (67)$$

Thus, we have  $(1/2\sqrt{\tilde{N}_1 \tilde{N}_2})[\text{Tr}(\mathbf{T}_2) + \text{Tr}(\tilde{\mathbf{T}}_1)] = \sum_{i=1}^K |c_i| = \|\tilde{\mathbf{X}}\|_{\mathbb{A}}$ . Since  $\{\mathbf{T}_2, \tilde{\mathbf{X}}, \tilde{\mathbf{T}}_1\}$  is a feasible solution to (51), we have  $\|\tilde{\mathbf{Y}}\|_{\mathbb{A}} \geq \tilde{p}$ .

We next prove  $\|\tilde{\mathbf{Y}}\|_{\mathbb{A}} \leq \tilde{p}$ . First, consider an auxiliary problem that is formulated to facilitate the proof. Let  $\hat{\mathbf{X}}^f = \sum_{i=1}^r c_i \mathbf{p}_{\omega_i}^f \mathbf{z}_2(\omega_{2i}) \mathbf{a}_1(f, -\omega_{1i})^H$  and  $\hat{\mathbf{X}} = [\hat{\mathbf{X}}^1, \dots, \hat{\mathbf{X}}^{N_f}]$ . A corresponding mapping operator  $\hat{\mathcal{R}}_d : \mathbb{C}^{N_2 \times N_1 N_f} \rightarrow \mathbb{C}^{N_2 \times N_1 N_f}$  can be constructed as

$$[\hat{\mathcal{R}}_d(\hat{\mathbf{X}})]_{i,j} = \hat{\mathbf{X}}_{(i-1)j+1,j} \quad (68)$$

such that  $\mathbf{Y} = \hat{\mathcal{R}}_d(\hat{\mathbf{X}})$ . An index selection matrix  $\mathbf{P} \in \mathbb{R}^{N_1 N_f, \tilde{N}_1 N_f}$  can also be constructed as

$$\mathbf{P}_{i,j} = \begin{cases} 1, & i = (f-1) \cdot N_1 + k \\ & j = (f-1) \cdot \tilde{N}_1 + (f-1)k + 1 \\ 0, & \text{otherwise} \end{cases} \quad (69)$$

such that

$$\mathbf{P} \cdot (\mathbf{p}_{\omega_i} \otimes \mathbf{z}_1(\omega_{1i})) = [p_{\omega_i}^1 \mathbf{a}_1(1, \omega_{1i})^T, \dots, p_{\omega_i}^{N_f} \mathbf{a}_1(N_f, \omega_{1i})^T]^T. \quad (70)$$

The auxiliary problem is formulated as follows:

$$\begin{aligned} \hat{p} &= \min_{\mathbf{T}_2, \hat{\mathbf{T}}_1, \hat{\mathbf{X}}} \frac{1}{2\sqrt{\tilde{N}_1 \tilde{N}_2}} [\text{Tr}(\mathbf{T}_2) + \text{Tr}(\hat{\mathbf{T}}_1)] \\ \text{s.t. } &\begin{bmatrix} \mathbf{T}_2 & \hat{\mathbf{X}} \\ \hat{\mathbf{X}}^H & \hat{\mathbf{T}}_1 \end{bmatrix} \succcurlyeq 0 \\ &\mathbf{Y} = \hat{\mathcal{R}}_d(\hat{\mathbf{X}}) \end{aligned} \quad (71)$$

where  $\mathbf{T}_2$  is a Toeplitz matrix,  $\hat{\mathbf{T}}_1$  is an  $N_f \times N_f$  block matrix with each block be an  $\tilde{N}_1 \times \tilde{N}_1$  Toeplitz matrix, and  $\hat{\mathbf{T}}_1 = \mathbf{P} \tilde{\mathbf{T}}_1 \mathbf{P}^H$ . The following lemma tells that  $\hat{p} = \|\tilde{\mathbf{Y}}\|_{\mathbb{A}}$ .

*Lemma 1:* Under the hypothesis of Theorem 1,  $\hat{p} = \|\tilde{\mathbf{Y}}\|_{\mathbb{A}}$ .

*Proof of Lemma 1:* We first prove  $\hat{p} \leq \|\tilde{\mathbf{Y}}\|_{\mathbb{A}}$ . A feasible solution to (71) can be constructed as follows:

$$\begin{aligned} \mathbf{T}_2 &= \sum_{i=1}^K |c_{2i}|^2 \mathbf{z}_2(\omega_{2i}) \mathbf{z}_2(\omega_{2i})^H \\ \hat{\mathbf{T}}_1 &= \sum_{i=1}^K |c_{1i}|^2 (\mathbf{P} \cdot \mathbf{p}_{\omega_i}^* \otimes \mathbf{z}_1(-\omega_{1i})) (\mathbf{P} \cdot \mathbf{p}_{\omega_i}^* \otimes \mathbf{z}_1(-\omega_{1i}))^H \\ \hat{\mathbf{X}} &= \sum_{i=1}^K c_{2i} c_{1i}^* \mathbf{z}_2(\omega_{2i}) \mathbf{P} \cdot \mathbf{p}_{\omega_i}^T \otimes \mathbf{z}_1(-\omega_{1i})^H \end{aligned} \quad (72)$$

where  $c_{1i} = \sqrt{|c_i|} \cdot (\tilde{N}_2/N_1)^{1/4}$ ,  $c_{2i} = \sqrt{|c_i|} \cdot \text{sign}(c_i) \cdot (N_1/\tilde{N}_2)^{1/4}$ . It is easy to verify that  $\mathbf{Y} = \hat{\mathcal{R}}_d(\hat{\mathbf{X}})$  and

$$\begin{bmatrix} \mathbf{T}_2 & \hat{\mathbf{X}} \\ \hat{\mathbf{X}}^H & \hat{\mathbf{T}}_1 \end{bmatrix} = \sum_{i=1}^K \begin{bmatrix} c_{2i} \mathbf{z}_2(\omega_{2i}) \\ c_{1i} \mathbf{P} \cdot \mathbf{p}_{\omega_i}^* \otimes \mathbf{z}_1(-\omega_{1i}) \end{bmatrix} \cdot \begin{bmatrix} c_{2i} \mathbf{z}_2(\omega_{2i}) \\ c_{1i} \mathbf{P} \cdot \mathbf{p}_{\omega_i}^* \otimes \mathbf{z}_1(-\omega_{1i}) \end{bmatrix}^H \succcurlyeq 0. \quad (73)$$

We have  $\text{Tr}(\mathbf{T}_2) = \sum |c_i| \sqrt{N_1 \tilde{N}_2}$  and

$$\begin{aligned} \text{Tr}(\hat{\mathbf{T}}_1) &= \text{Tr}(\mathbf{P} \tilde{\mathbf{T}}_1 \mathbf{P}^H) \\ &= \sum |c_i| \sqrt{\frac{\tilde{N}_2}{N_1}} \text{Tr} \left( \left[ p_{\omega_i}^1 \mathbf{a}_1(1, \omega_{1i})^T, \dots, p_{\omega_i}^{N_f} \mathbf{a}_1(N_f, \omega_{1i})^T \right]^T \right. \\ &\quad \left. \left[ p_{\omega_i}^1 \mathbf{a}_1(1, \omega_{1i})^T, \dots, p_{\omega_i}^{N_f} \mathbf{a}_1(N_f, \omega_{1i})^T \right]^* \right) \\ &= \sum |c_i| \sqrt{\frac{\tilde{N}_2}{N_1}} \sum |p_{\omega_i}^f|^2 \cdot N_1 \\ &= \sum |c_i| \sqrt{N_1 \tilde{N}_2}. \end{aligned} \quad (74)$$

Thus, we have  $\text{Tr}(\mathbf{T}_2) + \text{Tr}(\hat{\mathbf{T}}_1)/2\sqrt{N_1 \tilde{N}_2} = \sum |c_i| = \|\tilde{\mathbf{Y}}\|_{\mathbb{A}}$ , which indicates that  $\hat{p} \leq \|\tilde{\mathbf{Y}}\|_{\mathbb{A}}$ .

We next show that  $\hat{p} \geq \|\tilde{\mathbf{Y}}\|_{\mathbb{A}}$ . Define the 1-D atomic set  $\mathbb{A}_2$  as  $\mathbb{A}_2 = \{\mathbf{a}_2(1, \omega_2), \mathbf{a}_2(2, \omega_2), \dots, \mathbf{a}_2(N_f, \omega_2)\} * \mathbf{S}^T | \omega_2 \in [0, 1], \|\mathbf{S}\|_F = 1$ . Since the true spatial angular frequencies  $\{\omega_{2i}\}_{i=1}^{K_2}$  can be correctly estimated from signal  $\mathbf{Y}_2$  via 1-D



MMV-MFANM proposed in [33], the atomic decomposition of  $\mathbf{Y}_2$  with respect to  $\mathbb{A}_2$  is

$$\begin{aligned} \mathbf{Y}_2 &= \sum_{i=1}^K c_i [\mathbf{a}_2(1, \omega_{2i}) \mathbf{a}_1(1, \omega_{1i})^T p_{\omega_i}^1 | \dots | \\ &\quad \mathbf{a}_2(N_f, \omega_{2i}) \mathbf{a}_1(N_f, \omega_{1i})^T p_{\omega_i}^{N_f}] \\ &= \sum_{i=1}^K c_i \sqrt{N_1} \left[ \mathbf{a}_2(1, \omega_{2i}) \frac{\mathbf{a}_1(1, \omega_{1i})^T}{\|\mathbf{a}_1(1, \omega_{1i})\|} p_{\omega_i}^1 | \dots | \right. \\ &\quad \left. \mathbf{a}_2(N_f, \omega_{2i}) \frac{\mathbf{a}_1(N_f, \omega_{1i})^T}{\|\mathbf{a}_1(N_f, \omega_{1i})\|} p_{\omega_i}^{N_f} \right]. \end{aligned} \quad (75)$$

Thus  $\|\mathbf{Y}_2\|_{\mathbb{A}_2} = \sum_{i=1}^K c_i \sqrt{N_1} = \sqrt{N_1} \|\tilde{\mathbf{Y}}\|_{\mathbb{A}}$ . According to [33]

$$\begin{aligned} \|\mathbf{Y}_2\|_{\mathbb{A}_2} &= \min_{\mathbf{T}_2, \mathbf{W}, \hat{\mathbf{X}}} \frac{1}{2\sqrt{N_2}} [\text{Tr}(\mathbf{T}_2) + \text{Tr}(\mathbf{W})] \\ \text{s.t. } &\begin{bmatrix} \mathbf{T}_2 & \hat{\mathbf{X}} \\ \hat{\mathbf{X}}^H & \mathbf{W} \end{bmatrix} \succcurlyeq 0 \\ &\mathbf{Y} = \hat{\mathcal{R}}_d(\hat{\mathbf{X}}) \end{aligned} \quad (76)$$

where  $\mathbf{T}_2$  is a Toeplitz matrix. Compare (76) with (71), we have  $\hat{p} \geq \sqrt{N_1} \|\mathbf{Y}_2\|_{\mathbb{A}_2}$ . Recall that  $\|\mathbf{Y}_2\|_{\mathbb{A}_2} = \sqrt{N_1} \|\tilde{\mathbf{Y}}\|_{\mathbb{A}}$ , thus  $\hat{p} \geq \|\tilde{\mathbf{Y}}\|_{\mathbb{A}}$ .

To sum up,  $\hat{p} = \|\tilde{\mathbf{Y}}\|_{\mathbb{A}}$ . ■

Let  $\{\tilde{\mathbf{X}}_0, \tilde{\mathbf{T}}_{20}, \tilde{\mathbf{T}}_{10}\}$  be a feasible solution to (51). Let

$$\begin{aligned} \hat{\mathbf{X}}_0 &= \tilde{\mathbf{X}}_0 \mathbf{P}^H \\ \mathbf{T}_{20} &= \tilde{\mathbf{T}}_{20} \cdot \sqrt{N_1/\tilde{N}_1} \\ \hat{\mathbf{T}}_{10} &= \mathbf{P} \tilde{\mathbf{T}}_{10} \mathbf{P}^H \sqrt{\tilde{N}_1/N_1}. \end{aligned} \quad (77)$$

It is trivial that  $\mathbf{Y} = \hat{\mathcal{R}}_d(\hat{\mathbf{X}}_0)$ , and

$$\begin{bmatrix} \mathbf{T}_{20} & \hat{\mathbf{X}}_0 \\ \hat{\mathbf{X}}_0^H & \hat{\mathbf{T}}_{10} \end{bmatrix} = \begin{bmatrix} \tilde{\mathbf{T}}_{20} \cdot \sqrt{N_1/\tilde{N}_1} & \tilde{\mathbf{X}}_0 \mathbf{P}^H \\ \mathbf{P} \tilde{\mathbf{X}}_0^H & \mathbf{P} \tilde{\mathbf{T}}_{10} \mathbf{P}^H \sqrt{\tilde{N}_1/N_1} \end{bmatrix} \quad (78)$$

$\forall [x_1^H, x_2^H]^H$ , we have

$$\begin{aligned} &[x_1^H, x_2^H] \begin{bmatrix} \mathbf{T}_{20} & \hat{\mathbf{X}}_0 \\ \hat{\mathbf{X}}_0^H & \hat{\mathbf{T}}_{10} \end{bmatrix} [x_1^H, x_2^H]^H \\ &= \begin{bmatrix} \frac{N_1}{\tilde{N}_1} x_1^H, \frac{\tilde{N}_1}{N_1} x_2^H \end{bmatrix} \begin{bmatrix} \tilde{\mathbf{T}}_{20} & \tilde{\mathbf{X}}_0 \\ \tilde{\mathbf{X}}_0^H & \tilde{\mathbf{T}}_{10} \end{bmatrix} \begin{bmatrix} \frac{N_1}{\tilde{N}_1} x_1^H, \frac{\tilde{N}_1}{N_1} x_2^H \end{bmatrix}^H \\ &\geq 0. \end{aligned} \quad (79)$$

Thus  $\begin{bmatrix} \mathbf{T}_{20} & \hat{\mathbf{X}}_0 \\ \hat{\mathbf{X}}_0^H & \hat{\mathbf{T}}_{10} \end{bmatrix} \succcurlyeq 0$ , which indicates that  $\{\hat{\mathbf{X}}_0, \mathbf{T}_{20}, \hat{\mathbf{T}}_{10}\}$  is a feasible solution to (71). In other words, every feasible solution to (51) corresponds to a feasible solution to (71). It can be verified that  $\hat{p}_0 = (\text{Tr}(\mathbf{T}_{20}) + \text{Tr}(\hat{\mathbf{T}}_{10}))/2\sqrt{N_1\tilde{N}_2} = (\text{Tr}(\mathbf{T}_{20}) + \text{Tr}(\hat{\mathbf{T}}_{10}))/2\sqrt{N_1\tilde{N}_2} = \hat{p}_0$ . As a consequence,  $\hat{p} \geq \hat{p}_0$ . Together with  $\hat{p} = \|\tilde{\mathbf{Y}}\|_{\mathbb{A}}$ , we have  $\hat{p} \geq \|\tilde{\mathbf{Y}}\|_{\mathbb{A}}$ . Finally, we conclude that  $\hat{p} = \|\tilde{\mathbf{Y}}\|_{\mathbb{A}}$ . ■

## REFERENCES

- [1] *Optimum Array Processing*. Hoboken, NJ, USA: Wiley, 2002. [Online]. Available: <https://onlinelibrary.wiley.com/doi/abs/10.1002/0471221104.ch1>
- [2] J. Yang, Y. Yang, and B. Lei, "An efficient compressed sensing-based DOA estimation method in nested MIMO sonar," in *Proc. OCEANS-Aberdeen*, Jun. 2017, pp. 1–4.
- [3] L. Wang, C. Ren, and Z. Zheng, "DOA estimation for monostatic coprime MIMO radar with mixed-resolution quantization," *IEEE Trans. Veh. Technol.*, vol. 72, no. 12, pp. 16737–16741, Dec. 2023.
- [4] W. Zhai, X. Wang, X. Wang, M. Amin, and T. Shan, "Optimal sparse MIMO transceiver design for joint automotive sensing and communications," in *Proc. IEEE Int. Conf. Acoust., Speech, Signal Process. Workshops (ICASSPW)*, Jun. 2023, pp. 1–5.
- [5] U. Firat and T. Akgül, "Compressive beamforming for direction-of-arrival estimation of cyclostationary propeller noise," *Signal Process.*, vol. 214, Jan. 2024, Art. no. 109221. [Online]. Available: <https://www.sciencedirect.com/science/article/pii/S0165168423002955>
- [6] L. Li, Y. Chen, B. Zang, and L. Jiang, "A high-precision two-dimensional DOA estimation algorithm with parallel coprime array," *Circuits, Syst., Signal Process.*, vol. 41, no. 12, pp. 6960–6974, Dec. 2022, doi: 10.1007/s00034-022-02102-7.
- [7] M. Wax, T.-J. Shan, and T. Kailath, "Spatio-temporal spectral analysis by eigenstructure methods," *IEEE Trans. Acoust., Speech, Signal Process.*, vol. ASSP-32, no. 4, pp. 817–827, Aug. 1984.
- [8] H. Wang and M. Kaveh, "Coherent signal-subspace processing for the detection and estimation of angles of arrival of multiple wide-band sources," *IEEE Trans. Acoust., Speech, Signal Process.*, vol. 33, no. 4, pp. 823–831, Aug. 1985.
- [9] H. Hung and M. Kaveh, "Focussing matrices for coherent signal-subspace processing," *IEEE Trans. Acoust., Speech, Signal Process.*, vol. 36, no. 8, pp. 1272–1281, Aug. 1988.
- [10] Y. Chi and M. F. Da Costa, "Harnessing sparsity over the continuum: Atomic norm minimization for superresolution," *IEEE Signal Process. Mag.*, vol. 37, no. 2, pp. 39–57, Mar. 2020.
- [11] M. Huan, J. Liang, Y. Wu, Y. Li, and W. Liu, "SASA: Super-resolution and ambiguity-free sparse array geometry optimization with aperture size constraints for MIMO radar," *IEEE Trans. Antennas Propag.*, vol. 71, no. 6, pp. 4941–4954, Mar. 2023.
- [12] R. O. Schmidt, "A signal subspace approach to multiple emitter location and spectral estimation," Ph.D. dissertation, Stanford Univ., Stanford, CA, USA, 1982.
- [13] R. Schmidt, "Multiple emitter location and signal parameter estimation," *IEEE Trans. Antennas Propag.*, vol. AP-34, no. 3, pp. 276–280, Mar. 1986.
- [14] A. Paulraj, R. Roy, and T. Kailath, "A subspace rotation approach to signal parameter estimation," *Proc. IEEE*, vol. 74, no. 7, pp. 1044–1046, Jul. 1986.
- [15] Y. Hua, "Estimating two-dimensional frequencies by matrix enhancement and matrix pencil," *IEEE Trans. Signal Process.*, vol. 40, no. 9, pp. 2267–2280, Sep. 1992.
- [16] Y. Hua, "A pencil-MUSIC algorithm for finding two-dimensional angles and polarizations using crossed dipoles," *IEEE Trans. Antennas Propag.*, vol. 41, no. 3, pp. 370–376, Mar. 1993.
- [17] M. Haardt, M. D. Zoltowski, C. P. Mathews, and J. Nosske, "2D unitary ESPRIT for efficient 2D parameter estimation," in *Proc. Int. Conf. Acoust., Speech, Signal Process.*, vol. 3, 1995, pp. 2096–2099.
- [18] E. J. Candes, J. Romberg, and T. Tao, "Robust uncertainty principles: Exact signal reconstruction from highly incomplete frequency information," *IEEE Trans. Inf. Theory*, vol. 52, no. 2, pp. 489–509, Feb. 2006.
- [19] E. J. Candès, J. K. Romberg, and T. Tao, "Stable signal recovery from incomplete and inaccurate measurements," *Commun. Pure Appl. Math.*, vol. 59, no. 8, pp. 1207–1223, Aug. 2006. [Online]. Available: <https://onlinelibrary.wiley.com/doi/abs/10.1002/cpa.20124>
- [20] Z. Yang, J. Li, P. Stoica, and L. Xie, "Sparse methods for direction-of-arrival estimation," in *Academic Press Library in Signal Processing*, vol. 7, R. Chellappa and S. Theodoridis, Eds., New York, NY, USA: Academic, 2018, ch. 1, pp. 509–581. [Online]. Available: <https://www.sciencedirect.com/science/article/pii/B9780128118870000110>
- [21] Z. Tang, G. Blacquiere, and G. Leus, "Aliasing-free wideband beamforming using sparse signal representation," *IEEE Trans. Signal Process.*, vol. 59, no. 7, pp. 3464–3469, Jul. 2011.
- [22] Z.-M. Liu, Z.-T. Huang, and Y.-Y. Zhou, "Sparsity-inducing direction finding for narrowband and wideband signals based on array covariance vectors," *IEEE Trans. Wireless Commun.*, vol. 12, no. 8, pp. 1–12, Aug. 2013.
- [23] Y. Chi, A. Pezeshki, L. Scharf, and R. Calderbank, "Sensitivity to basis mismatch in compressed sensing," in *Proc. IEEE Int. Conf. Acoust., Speech Signal Process.*, Mar. 2010, pp. 3930–3933.

- [24] G. Zhang, H. Liu, W. Dai, T. Huang, Y. Liu, and X. Wang, "Passive joint emitter localization with sensor self-calibration," *Remote Sens.*, vol. 15, no. 3, p. 671, Jan. 2023. [Online]. Available: <https://www.mdpi.com/2072-4292/15/3/671>
- [25] A. Fannjiang and H.-C. Tseng, "Compressive radar with off-grid targets: A perturbation approach," *Inverse Problems*, vol. 29, no. 5, Apr. 2013, Art. no. 054008, doi: [10.1088/0266-5611/29/5/054008](https://doi.org/10.1088/0266-5611/29/5/054008).
- [26] Q. Guo, Z. Xin, T. Zhou, and S. Xu, "Off-grid space alternating sparse Bayesian learning," *IEEE Trans. Instrum. Meas.*, vol. 72, pp. 1–10, 2023.
- [27] V. Chandrasekaran, B. Recht, P. A. Parrilo, and A. S. Willsky, "The convex geometry of linear inverse problems," *Found. Comput. Math.*, vol. 12, pp. 805–849, Oct. 2012, doi: [10.1007/s10208-012-9135-7](https://doi.org/10.1007/s10208-012-9135-7).
- [28] E. J. Candès and C. Fernandez-Granda, "Towards a mathematical theory of super-resolution," *Commun. Pure Appl. Math.*, vol. 67, no. 6, pp. 906–956, 2014. [Online]. Available: <https://onlinelibrary.wiley.com/doi/abs/10.1002/cpa.21455>
- [29] G. Tang, B. Bhaskar, P. Shah, and B. Recht, "Compressed sensing off the grid," *IEEE Trans. Inf. Theory*, vol. 59, no. 11, pp. 7465–7490, Nov. 2013.
- [30] Y. Chi and Y. Chen, "Compressive two-dimensional harmonic retrieval via atomic norm minimization," *IEEE Trans. Signal Process.*, vol. 63, no. 4, pp. 1030–1042, Feb. 2015.
- [31] Z. Yang, L. Xie, and P. Stoica, "Vandermonde decomposition of multilevel Toeplitz matrices with application to multidimensional super-resolution," *IEEE Trans. Inf. Theory*, vol. 62, no. 6, pp. 3685–3701, Jun. 2016.
- [32] Y. Wu, M. B. Wakin, and P. Gerstoft, "Gridless DOA estimation with multiple frequencies," *IEEE Trans. Signal Process.*, vol. 71, pp. 417–432, 2023.
- [33] Y. Wu, M. B. Wakin, and P. Gerstoft, "Non-uniform array and frequency spacing for regularization-free gridless DOA," *IEEE Trans. Signal Process.*, vol. 72, pp. 2006–2020, 2024.
- [34] B. Dumitrescu, *Positive Trigonometric Polynomials and Signal Processing Applications*. Cham, Switzerland: Springer, 2007.
- [35] Y. Jiang, D. Li, X. Wu, and W.-P. Zhu, "A gridless wideband DOA estimation based on atomic norm minimization," in *Proc. IEEE 11th Sensor Array Multichannel Signal Process. Workshop (SAM)*, Jun. 2020, pp. 1–5.
- [36] M. J. Jirhandeh, H. Hezaveh, and M. H. Kahaei, "Super-resolution DOA estimation for wideband signals using non-uniform linear arrays with no focusing matrix," *IEEE Wireless Commun. Lett.*, vol. 11, no. 3, pp. 641–644, Mar. 2022.
- [37] M. Grant and S. Boyd. (2014). *CVX: MATLAB Software for Disciplined Convex Programming*. [Online]. Available: <https://cvxr.com/cvx>
- [38] S. Nannuru, K. L. Gamba, and P. Gerstoft, "Sparse Bayesian learning with multiple dictionaries," in *Proc. IEEE Global Conf. Signal Inf. Process. (GlobalSIP)*, Nov. 2017, pp. 1190–1194.
- [39] Y. Kase, T. Nishimura, T. Ohgane, Y. Ogawa, T. Sato, and Y. Kishiyama, "Accuracy improvement in DOA estimation with deep learning," *IEICE Trans. Commun.*, vol. 105, no. 5, pp. 588–599, 2022.
- [40] D. Santos-Domínguez, S. Torres-Guijarro, A. Cardenal-López, and A. Pena-Gimenez, "ShipsEar: An underwater vessel noise database," *Appl. Acoust.*, vol. 113, pp. 64–69, Dec. 2016. [Online]. Available: <https://www.sciencedirect.com/science/article/pii/S0003682X16301566>
- [41] I.-C. Chern, S. Chern, H.-C. Kuo, H.-H. Tseng, K.-H. Hung, and Y. Tsao, "Voice direction-of-arrival conversion," in *Proc. IEEE 33rd Int. Workshop Mach. Learn. Signal Process. (MLSP)*, Sep. 2023, pp. 1–6.
- [42] R. Scheibler, E. Bezzam, and I. Dokmanić, "Pyroomacoustics: A Python package for audio room simulation and array processing algorithms," in *Proc. IEEE Int. Conf. Acoust. Speech Signal Process. (ICASSP)*, Calgary, AB, Canada, Apr. 2018, pp. 351–355.



**Jingming Zhang** received the B.Eng. degree in electronic science and technology from Hohai University, Nanjing, China, in 2022. He is currently pursuing the M.Eng. degree in signal and information processing with the Institute of Acoustics, Chinese Academy of Sciences, Beijing, China.

His research interests include array signal processing and sparse signal processing.



**Min Wu** (Senior Member, IEEE) received the bachelor's degree in information countermeasure and the Ph.D. degree in signal processing from the State Key Laboratory of Radar Signal Processing, Xidian University, Xi'an, China, in 2011 and 2016, respectively.

From 2014 to 2015, she held a visiting position with the Department of Electrical and Computer Engineering, University of Delaware, Newark, DE, USA. Since 2016, she has been the Faculty with the Institute of Acoustics, Chinese Academy of Sciences, Beijing, China, first as an Assistant Professor, from 2016 to 2022, and, then as an Associate Professor, since 2022. She has presided over many projects, such as the National Natural Science Foundation of China Program, the Innovation-Seeking Program of Chinese Academy of Sciences, and the Key Laboratory Program of Chinese Academy of Sciences. Her research interests include array signal processing, radar/sonar parameter estimation, and super-resolution imaging.



**Chengpeng Hao** (Senior Member, IEEE) received the B.S. and M.S. degrees in electronic engineering from Beijing Broadcasting Institute, Beijing, China, in 1998 and 2001, respectively, and the Ph.D. degree in signal and information processing from the Institute of Acoustics, Chinese Academy of Sciences (IACAS), Beijing, in 2004.

From 2013 to 2014, he held a visiting position with the Department of Electrical and Computer Engineering, Queens University, Kingston, ON, Canada. He is currently a Full Professor with IACAS. Since 2021, he serves as the Director of Unmanned Underwater Vehicles (UUV) Lab of IACAS. He has authored or co-authored more than 180 journals and conference papers. His research interests include statistical signal processing, array signal processing and UUV design.

He is currently an Associate Editor of *IEEE SIGNAL PROCESSING LETTERS* and *Signal, Image and Video Processing* (Springer).



**Yongqing Wu** (Senior Member, IEEE) received the B.Sc. degree in communication engineering from Xidian University, Xi'an, China, in 1990, the M.Sc. degree in computer application from Hebei University of Technology, Tianjin, China, in 1998, and the Ph.D. degree in precision instrument from Tianjin University, Tianjin, in 2001.

His experience includes two periods from 1990 to 1995 at Tianjin LuHai Land and Ocean Petroleum Equipment System Engineering Company Ltd., Tianjin, China, as an Engineer conducting Research and Development in intelligent automatic instruments. He was a Post-Doctoral Research Associate with the Institute of Acoustics, Chinese Academy of Sciences (IACAS), Beijing, China, from 2001 to 2003, joined IACAS in 2003, and became a Professor in 2011. He is also a Professor with the University of Chinese Academy of Sciences, Beijing, as a Lecturer in giving courses on underwater acoustics and signal processing. His main research interests include underwater acoustic positioning and navigation, underwater target detection and recognition, and their applications.